

1
2
3
4
5
6
7
8
9
10
11
12
13
14
15
16
17
18
19
20
21
22
23

Timescales and rates of intrusive and metamorphic processes determined from zircon and garnet in migmatitic granulite, Fiordland, New Zealand

HAROLD STOWELL¹, JOSHUA SCHWARTZ², ELIZABETH BOLLEN¹, ANDY TULLOCH³, JAHANDAR RAMEZANI⁴, KEITH KLEPEIS⁵

¹Geological Sciences, University of Alabama, Tuscaloosa, AL 35487-0338 USA

²Geological Sciences, California State University Northridge, Northridge, CA 91330 USA

³GNS Science 764 Cumberland St., Dunedin 9016, Private Bag 1930, Dunedin 9054, New Zealand

⁴Earth, Atmospheric and Planetary Science, Massachusetts Institute of Technology, Cambridge, MA 02139, USA

⁵Department of Geology, University of Vermont, 180 Colchester Ave., Burlington, Vermont 05405, USA

ABSTRACT

Zircon U-Pb, and garnet Sm-Nd and Lu-Hf dates provide important constraints on local and orogenic scale processes in lower-crustal rocks. However, in high-temperature metamorphic rocks these isotopic systems typically yield significant ranges reflecting both igneous and metamorphic processes. Therefore, linking dates to specific aspects of rock history can be problematic. In Fiordland New Zealand, granulite-facies orthogneiss is cut by leucosomes that are bordered by garnet clinopyroxene reaction zones (garnet reaction zones). In both host orthogneiss and garnet reaction zones, zircon are typically anhedral with U-Pb dates ranging from 118.30±0.13 to 115.70±0.18 Ma (CA-ID-TIMS) and 121.4±2.0 to 109.8±1.8 Ma

24 (SHRIMP-RG). Zircon dates in host and garnet reaction zone do not define distinct populations.
25 In addition, the dates cannot be readily grouped based on external morphology or internal CL
26 zoning. Zircon trace-element concentrations indicate two distinct crystallization trends, clearly
27 seen in Th and U, which are interpreted to reflect evolution of separate magma batches. Garnet
28 occurs in selvages to the leucosome veins and in the adjacent garnet reaction zones. In selvages
29 and host orthogneiss, garnet is generally 0.5 to 1 cm diameter and euhedral, and is 0.1 to 0.5 cm
30 diameter and subhedral in garnet reaction zones. Garnet Sm-Nd and Lu-Hf dates range from ca.
31 115 to 101 Ma (including uncertainties) and correlate with grain size. We interpret the CA-ID-
32 TIMS zircon dates to record the age of magma emplacement and the SHRIMP-RG dates to
33 record a range from igneous crystallization to metamorphic dissolution and reprecipitation and/or
34 local Pb loss. Zircon compositional trends within the garnet reaction zone and host are
35 compatible with locally isolated melt and/or separate intrusive magma batches for the two
36 samples described here. Dates for the largest, ~ 1 cm, garnet of ~ 113 Ma record growth during
37 metamorphism, while the smaller grains with younger dates reflect high temperature
38 intracrystalline diffusion and isotopic closure during cooling. The comprehensive
39 geochronological data set for a single location in the Malaspina Pluton illustrates a complex and
40 protracted geologic history common in granulite facies rocks, estimates lower crustal cooling
41 rates of ~ 20°C /m.y., and underlines the importance of multiple chronometers and careful
42 textural characterization for assigning meaningful ages to lower-crustal rocks. Numerous single
43 location datasets, like the one described here, are needed to evaluate the spatial extent and
44 variation of cooling rates for Fiordland and other lower crustal exposures.

45 **Keywords:** zircon U-Pb, garnet Sm-Nd, migmatite, lower crust, rates of intrusion, duration of
46 metamorphism

47

48

INTRODUCTION AND GEOLOGIC SETTING

49 Zircon and garnet isotopic dates are widely used for understanding local and orogenic scale

50 processes in magmatic arcs, lower-crustal rocks, and high-grade metamorphic terrains. For

51 example, ages and associated trace-element compositions in zircon are critical components of

52 studies that address magma sources, mixing, and assimilation (e.g., Hammerli et al., 2018).

53 Garnet stability is important for characterizing arc roots because it exerts controls on partial

54 melting processes, the composition of intermediate- to high- silica magmas found in magmatic

55 arcs (e.g., Lee et al., 2006; Ducea et al., 2015), and the density of lower crust and mantle

56 lithosphere (e.g., Kay and Mahlburg Kay, 1993). Garnet ages provide a means of understanding

57 processes in magmatic arc roots because they can be directly linked to pressure and temperature

58 estimates for constructing quantitative P-T-t paths and calculating rates of tectonic processes

59 (e.g., Stowell et al., 2001; Lapen et al., 2003; Stowell et al., 2007; Gatewood et al., 2015). In

60 granulite facies metamorphic rocks, the zircon U-Pb, and garnet Sm-Nd and Lu-Hf ages

61 generally yield significant differences that may reflect igneous, peak metamorphic, and post-

62 peak metamorphic processes (e.g., Mezger et al., 1992; Hoskin, 2003; Harley et al., 2007; Baxter

63 and Scherer, 2013; Smit et al., 2013, 2014; Baxter et al., 2017). For example, Yakymchuk and

64 Brown (2014) used phase equilibria modeling to infer that partially melted granulite may contain

65 multiple generations of zircon, some of which may predate metamorphism and others which

66 grew during decreasing temperature after the metamorphic peak. The age ranges from each

67 chronometer may be a challenge to interpret, but if interpretation is possible the results can

68 provide quantitative ages for numerous points in a rock's history. This in turn provides the data

69 for calculating heating and cooling rates in the lower crust.

70 Fiordland is an ideal location for studying lower crustal processes because it is comprised of
71 a mid- to lower-crustal section of a continental magmatic arc that was active along the
72 Gondwana margin from the late Paleozoic (Tulloch et al. 2009; Turnbull et al. 2016) to the
73 Cretaceous (Mattinson et al., 1986; Klepeis et al., 2003; Tulloch and Kimbrough, 2003).
74 Fiordland is dominated by paired belts of older mid-crustal plutons on the east (outboard;
75 predominantly Darran suite) and younger lower crustal plutons on the west (inboard; Tulloch and
76 Kimbrough, 2003). The western magmatic belt in northern and central Fiordland is dominated by
77 Cretaceous plutons of the Western Fiordland Orthogneiss (WFO). These diorite to monzodiorite
78 plutons intruded between 128 and 114 Ma based on zircon U-Pb geochronology using Sensitive
79 High Resolution Ion Microprobe (SHRIMP) and laser ablation inductively-coupled plasma mass
80 spectrometry (LA-ICPMS) analysis (e.g. Hollis et al., 2004; Milan et al., 2016; Schwartz et al.,
81 2017; Decker et al., 2017) and 123 to 117 Ma based on TIMS zircon geochronology (Mattinson
82 et al., 1986; Tulloch and Kimbrough, 2003). The Malaspina Pluton is the southernmost of the
83 three largest WFO plutons (Fig. 1) and laser ablation U-Pb zircon ages range from 114 to 117
84 Ma (e.g., Hollis et al., 2004; Stowell et al., 2014; Milan et al., 2016). Large parts of the WFO,
85 including much of the Malaspina Pluton, were metamorphosed to garnet granulite conditions ca.
86 112 Ma based on garnet Sm-Nd geochronology (Stowell et al., 2014, 2017). Granulite
87 metamorphism occurred at 12 to 13.5 kbar and temperatures in excess of 850°C (Oliver, 1977,
88 1980; Bradshaw, 1989; Dazcko and Halpin, 2009; Stowell et al., 2014) after eclogite
89 metamorphism in the Breaksea area (Stowell et al., 2017). Granulite metamorphism locally
90 produced garnet and clinopyroxene mineral assemblages that are commonly associated with
91 leucocratic partial melts. In the WFO, post granulite *composite* cooling rates of ~ 50°C/m.y.

92 (Flowers et al., 2005) and 8-14°C m.y. (Schwartz et al., 2016) have been estimated from U-Pb
93 ages and metamorphic temperatures obtained from multiple sample locations.

94 The mid- to lower- crust of magmatic arcs may have numerous textural occurrences of garnet
95 and some of these are commonly in plutonic rocks (e.g., Stevenson et al., 2005; Hacker et al.,
96 2008; Jagoutz, 2010). In plutonic rocks, metamorphic garnet ± clinopyroxene may replace
97 igneous minerals adjacent to cross cutting and pervasive leucosomes, forming what we refer to
98 here as garnet reaction zones. These garnet reaction zones are widespread in migmatite
99 throughout northern and central Fiordland (e.g., Blattner, 1976; Oliver, 1977; Clarke et al., 2005;
100 Daczko et al., 2016). The eastern Malaspina Pluton in central Fiordland is partly recrystallized to
101 garnet granulite (Oliver, 1980; Turnbull et al., 2010) and lies structurally below the Doubtful
102 Sound shear zone (Fig. 1)(Oliver and Coggon, 1979; Gibson and Ireland, 1995). This shear zone
103 separates the pluton from dominantly metasedimentary rocks of the overlying Deep Cove Gneiss
104 and it has been interpreted as an extensional fault Gibson et al. (1988). The garnet reaction zones
105 in the Malaspina Pluton are centimeters to meters in width, containing dominantly metamorphic
106 mineral assemblages with largely igneous mineral assemblages and textures outside the garnet
107 reaction zones. The Malaspina Pluton exposed along Crooked Arm (Fig. 1) includes extensive
108 areas of LS tectonites dominated by garnet reaction zones that are cut by 5 to 20 cm-wide
109 leucosomes. Locally, leucosome veins have distinct borders of coarse porphyroblasts referred to
110 here as selvages. In the Crooked Arm area these are generally garnet selvages (Fig. 2). Garnet
111 occurrences are classified according to Stowell et al. (2014): Type 1 garnet occurs in discrete
112 garnet reaction zones, Type 2 garnet forms planar to sub-planar arrays as selvages to
113 trondhjemite veins, and Type 3 garnet are porphyroblasts in diffuse leucosomes. Most or all
114 porphyroblastic and selvaige garnet must have grown during partial melting based on crystallized

115 melt inclusions and textures (Stowell et al., 2014). Garnet in the garnet reaction zones is directly
116 related to melts and/or fluids and has also been interpreted to have grown during partial melting
117 of the host gneiss (Oliver, 1977; Stowell et al., 2014); however, other researchers have inferred
118 that garnet growth in the garnet reaction zones resulted from dehydration of the host rock by
119 externally-derived trondhjemite magma (e.g. Clarke et al. 2005).

120 The outcrops along Crooked Arm are ideal for evaluating the rate of cooling from garnet
121 granulite metamorphic temperatures attained during the development of mylonite fabrics. We
122 present zircon U-Pb, garnet Sm-Nd, and garnet Lu-Hf ages, and trace-element mineral
123 compositions for a single outcrop of the Malaspina Pluton (Figs. 1 & 2). Syn- and post-magmatic
124 strain in much of the pluton (Klepeis et al., 2016), including rocks along Crooked Arm, and
125 metamorphism ca. 4 m.y. after emplacement, produced hornblende pyroxene plagioclase
126 orthogneiss with locally abundant garnet. Much of the orthogneiss is compositionally layered at a
127 1 to 10 m scale (Fig. 2) with rocks ranging from hornblendite to diorite and monzodiorite. These
128 thick layers are interpreted as igneous in origin. The central part of Crooked Arm is dominated
129 by high-temperature L-S tectonites (Stowell et al. 2014). High-temperature metamorphism with
130 local partial melting at $\sim 920^{\circ}\text{C}$ and 14 kbar resulted in diffuse and vein leucosomes that are
131 dominantly trondhjemite in composition (Stowell et al. 2014).

132 In this contribution, we evaluate zircon and garnet chronometers in granulite facies
133 migmatitic metabasite from Fiordland. The interpretations are based in part on published
134 pressure, temperature, and garnet Sm-Nd age data for metamorphism (Stowell et al., 2014). New
135 data include: additional garnet Sm-Nd ages, garnet Lu-Hf ages, new zircon U-Pb ages, and
136 zircon and garnet trace element concentrations. The trace element concentrations and zoning in
137 these minerals provides the context for interpreting the ages. The resulting history of pluton

138 intrusion, high temperature metamorphism, and partial melting is used to determine the
139 timescales for metamorphism and rates of heating and cooling for a single outcrop along
140 Crooked Arm.

141

142 ANALYTICAL METHODS

143 We compare geochronological data derived from the U-Pb isotopic system in zircon and the
144 Lu-Hf and Sm-Nd isotopic systems in garnet. The zircon U-Pb isotopic data were obtained by
145 secondary ion mass spectrometry (Sensitive High Resolution Ion Microprobe with Reverse
146 Geometry, or SHRIMP-RG) and by chemical abrasion isotope dilution thermal ionization mass
147 spectrometry (CA-ID-TIMS) on single zircon. The garnet isotopic data were obtained from
148 solution multi-collector ICPMS (Lu and Hf) and ID-TIMS (Sm and Nd).

149

150 Mineral compositional analysis

151 Quantitative major element mineral compositions and mineral zoning maps were obtained
152 from individual point analyses and electron beam rastering, respectively. X-ray maps and
153 quantitative point analyses were obtained on the JEOL 8600 electron probe microanalyzer
154 (EPMA) at the University of Alabama following methods described in Stowell et al. (2010). The
155 K_{α} X-ray maps were obtained using a Bruker energy dispersive spectrometer and Esprit software.
156 Quantitative point analyses were obtained using wavelength dispersive spectrometers, CitZAF
157 correction techniques, and Probe for EPMA software (Donovan, 2010). Major element data for
158 garnet and other phases was first qualitatively assessed with K_{α} X-ray maps and then quantified
159 as appropriate with point analyses and line scans. Inclusions and compromised analyses were

160 filtered out of the quantitative data. Additional information about EPMA methods and analytical
161 precision at the University of Alabama can be found in Stowell et al. (2010).

162 Quantitative spot analyses for trace elements in garnet were obtained by laser ablation
163 inductively-coupled plasma mass spectrometry (LA-ICPMS). Large garnet trace-element maps
164 were determined by Alan Koenig at the U.S. Geological Survey in Lakewood, CO. Analyses
165 were obtained with the CETAC LSX-500 coupled to a Perkin Elmer ELAN DRC-e inductively
166 coupled plasma mass spectrometer (ICP-MS). Instrument operating conditions: wavelength =
167 266 nm, energy = 9 mJ, spot size = 150 μm , pulse rate 10 sec⁻¹, carrier gas = 1.05 l/min Ar,
168 calibration standard = USGS GSE-1g, and 30 s ablation time. Raw intensity data were converted
169 to concentrations using the GeoPro offline data processing package. Calcium, determined by
170 EPMA, was used as an internal standard. Trace-element analyses from small garnet grains were
171 obtained at California State University Northridge. Analyses were obtained with a Teledyne-
172 CETAC Analyte G2 Ar-F₂ excimer LA system attached to a Thermo Element 2 ICP-MS.
173 Instrument operating conditions: wavelength = 193 nm, energy = 9 mJ, spot size = 40 μm , pulse
174 rate 10 sec⁻¹, carrier gas = 1.05 l/min He, calibration standards = USGS BHVO-2g and GSC-1g,
175 and 30 s ablation time. Raw intensity data were converted to concentrations using Iolite offline
176 data processing package (Paton et al., 2011). Calcium, determined by EPMA, was used as an
177 internal standard.

178 Quantitative spot analyses for trace-elements in zircon (Ti, Fe, Y, La, Ce, Nd, Sm, Eu, Gd,
179 Dy, Er, Yb, Hf, U, and Th) were obtained at the Stanford-USGS Micro-Analysis SHRIMP-RG
180 facility. These data were obtained simultaneously, from the same analytical volume used for
181 zircon U-Pb isotopic analyses. Trace element zircon standard MAD-1 (Coble et al., 2018) were
182 analyzed at the beginning of the analytical session. Operating conditions were the same as those

183 described below for zircon isotope analysis. Raw intensity data were normalized to count rates
184 for silica (measured as $^{28}\text{Si}^{16}\text{O}$) and converted to concentrations using SQUID-2 data processing
185 package (Ludwig, 2009). A more detailed discussion of these methods, including the standards
186 and analytical precision are reported in Schwartz et al. (2017).

187

188 **Zircon isotopic analysis**

189 Approximately 5 kg of fresh rock was collected from two samples from the outcrop shown in
190 Figure 2b for zircon geochronology. Heavy minerals were concentrated out of pulverized rock by
191 sequential use of a Gemini Table, high-density liquid (methylene iodide), and a Frantz magnetic
192 separator. Zircon grains were handpicked under a binocular microscope based on clarity and
193 physical intactness.

194 **Chemical abrasion isotope dilution thermal ionization mass spectrometry (CA-ID-**
195 **TIMS).** Zircon analysis by thermal-ionization mass spectrometry followed the detailed
196 procedures outlined in Ramezani et al. (2013) and involved pre-treatment by a chemical abrasion
197 method modified after Mattinson (2005) to minimize the effects of radioactive decay induced
198 crystal defects and associated Pb-loss. Zircon were heated in a furnace for 60 hours at 900°C.
199 The annealed grains were loaded into FEP Teflon microcapsules and leached in 29M HF at
200 210°C within a high-pressure vessel for 12 hours. The partially dissolved zircon grains were then
201 fluxed in 4M HNO₃ and 6M HCl solutions successively on a hot plate and in an ultrasonic bath
202 (1 hour each) and rinsed in between with several volumes of ultrapure water. Rinsed zircon were
203 then loaded individually into microcapsules with the EARTHTIME ET535 mixed ^{205}Pb - ^{233}U -
204 ^{235}U tracer solution (Condon et al., 2015; McLean et al., 2015) and 29M HF to completely
205 dissolve at 210°C for 48 hours. Pb and U were chemically separated using an HCl-based anion-

206 exchange chemistry after Krogh (1973) and loaded together with a silica gel emitter solution on
207 zone-refined and outgassed rhenium filaments. The Pb and U isotopic compositions were
208 measured on a VG Sector 54 multi-collector thermal ionization mass spectrometer at the
209 Massachusetts Institute of Technology Isotope Laboratory. Pb isotopes were measured by peak-
210 hopping on a Daly photomultiplier ion-counting detector, whereas U isotopes were measured as
211 oxides in a static mode using three Faraday collectors. Correction of isotopic ratios, calculation
212 of dates and propagation of uncertainties were completed using the computer applications Tripoli
213 and ET_Redux (Bowring et al., 2011; McLean et al., 2011). All single crystal age interpretations
214 are based on $^{206}\text{Pb}/^{238}\text{U}$ dates, which are reported at 95% confidence level.

215 **Sensitive High Resolution Ion Microprobe-Reverse Geometry (SHRIMP-RG).** Spot
216 analyses for uranium and lead isotope ratios were obtained at the Stanford-USGS Micro-
217 Analysis SHRIMP-RG facility. Epoxy mounts were gold coated to prevent charging during
218 analysis. Spots were chosen using reflected light and CL images (Fig. 3) based on zonation
219 patterns. Rims and distinct cores were chosen to compare ages. The Temora-2 standard was
220 analyzed after every 3-4 unknown analyses. The Temora-2 analyses during the analytical session
221 were reproducible with a 0.25% distribution about the mean. The primary O_2^- primary ion beam
222 generated analysis pits ~30 micrometers in diameter and ~2 micrometers deep, and sputtered
223 secondary ions were mass analyzed in five cycles through the mass table ($^{28}\text{Si}^{16}\text{O}$ to $^{238}\text{U}^{16}\text{O}$) for
224 each sample. Fractionation of Pb relative to Th and U, was corrected for by comparison of the
225 fractionation that occurred during analysis of the standard zircon. Common Pb was estimated
226 from the excess ^{207}Pb counts in the measured $^{207}\text{Pb}/^{206}\text{Pb}$ ratio for each analysis, assuming a Pb
227 isotopic composition from Stacey and Kramers (1975) models for average crustal Pb. Raw data
228 were reduced using SQUID-2 software (Ludwig, 2009), and all age calculations and Concordia

229 diagrams were made using IsoplotR (Vermeesch, 2018). Analyses with common Pb corrections
230 of >5% were discarded from further consideration. Zircon dates are reported using the common-
231 Pb corrected $^{206}\text{Pb}/^{238}\text{U}$ age. Individual spot ages and ages discussed in the text are presented
232 with 2σ uncertainties.

233

234 **Garnet isotopic analyses**

235 **Samarium and neodymium isotopes.** Methods for Sm-Nd garnet geochronology are
236 modified from those in Stowell et al. (2010 & 2014). A full description of the methods is
237 available online (<https://radis.as.ua.edu/radis-and-isopet-procedures/>). Garnet and clinopyroxene
238 were separated from the garnet reaction zone by crushing a section of rock containing only <2
239 mm garnet grains and then handpicking. These grains were crushed using a carbide steel mortar
240 and pestle and then manually picked under a binocular microscope to avoid mineral inclusions.
241 Additional inclusions were removed by leaching garnet with HF and HClO₄ acids (e.g.,
242 Gatewood et al., 2015). Whole rock and matrix were prepared from ~ 1 cm cubes of cut rock and
243 the matrix was separated by crushing and removing all garnet from one of the cubes. All of the
244 samples were then fully dissolved with HF and nitric acids in SAVILLEX PFA vials on a hot
245 plate. Sample aliquots were spiked with mixed Sm and Nd Spike B from the University of North
246 Carolina at Chapel Hill. REE fractions were separated and concentrated from samples using
247 disposable polyprep BioRad ion chromatography columns. Samarium and Nd splits were
248 separated from the REE fractions using methylactic acid (MLA) and custom-designed 23 cm
249 silica glass columns. Samarium isotopes were measured as metal and Nd isotopes measured as
250 oxide using the VG Sector 54 Thermal Ionization Mass Spectrometer (TIMS) in the Radiogenic
251 Isotope Laboratory (RadIs) at the University of Alabama. Neodymium isotope ratios were

252 normalized to $^{146}\text{Nd}/^{144}\text{Nd} = 0.7219$ and then used with Sm isotope values to compute final
253 isotope ratios and elemental concentrations by isotope dilution. The JNdi Nd standard was run as
254 an oxide periodically during data collection and the results were $^{143}\text{Nd}/^{144}\text{Nd} =$
255 0.512117 ± 0.000013 as compared to $^{143}\text{Nd}/^{144}\text{Nd} = 0.512115 \pm 0.000007$ reported by Tanaka et al.
256 (2000); therefore, no additional Nd isotope normalization was required. The Sm-Nd isochrons
257 were regressed using the decay constant of $6.540 \times 10^{-12} \text{ y}^{-1}$ for $\lambda^{147}\text{Sm}$ (Lugmair and Marti,
258 1978; Begemann and others, 2001). Sm-Nd isochrons were calculated and plotted with IsoplotR
259 (Vermeesch et al., 2018). The Sm-Nd large garnet age in Stowell et al. (2014), originally
260 calculated using Isoplot (Ludwig, 2012) was recalculated for this study using IsoplotR, resulting
261 in a 0.3 Ma age increase.

262 **Lutetium and hafnium isotopes.** Garnet separates and two whole rock powders – one
263 digested in a hydrothermal vessel and one digested on a hot plate – were analyzed for Lu-Hf
264 geochronology. The Lu and Hf isotope ratios were determined on a Thermo Scientific™
265 Neptune MC–ICP-MS in the Radiogenic Isotope and Geochronology Laboratory at Washington
266 State University. The detailed procedures for sample digestion, spiking, isotope analyses, and
267 data reduction are described in Vervoort et al. (2004) and Cheng et al. (2008). Hafnium isotopic
268 compositions were corrected for mass fractionation with an exponential law using $^{179}\text{Hf}/^{177}\text{Hf} =$
269 0.7325 , and normalized, over the course of this work, relative to $^{176}\text{Hf}/^{177}\text{Hf} = 0.282160$ for the
270 JMC475 Hf standard. External uncertainties applied to measured data for the purpose of data
271 regressions and age calculations are 0.5% for $^{176}\text{Lu}/^{177}\text{Hf}$, and a combination of 2σ in-run error
272 and a blanket 0.005% uncertainty added in quadrature for $^{176}\text{Hf}/^{177}\text{Hf}$. The Lu–Hf isochrons were
273 regressed using the decay constant of $1.867 \times 10^{-11} \text{ y}^{-1}$ for $\lambda^{176}\text{Lu}$ (Scherer et al., 2001,

274 Söderlund et al., 2004). Lu and Hf isochrons were calculated and plotted with IsoplotR
275 (Vermeesch et al., 2018).

276

277

RESULTS

278 Sampling for this study focused on the host pluton containing orthopyroxene, clinopyroxene,
279 hornblende, and plagioclase; a garnet reaction zone containing clinopyroxene, garnet, and
280 plagioclase; and garnet selvages along cross-cutting trondhjemite veins. Approximately 1 cm
281 garnet in the vein selvages (Type 2) are arranged in a planar fashion that typically comprise a
282 narrow array on both sides of the trondhjemite leucosomes (Fig. 2). Smaller, 0.05 to 0.2 cm
283 garnet are restricted to the garnet reaction zones (Type 1) and form monomineralic lenses and
284 intergrowths with clinopyroxene. Garnet in the selvages contains numerous rutile inclusions,
285 some of which are crystallographically aligned, and lesser abundances of clinopyroxene, apatite,
286 titanite, ilmenite, zircon, spinel, and plagioclase inclusions. Rare polyphase inclusions of albite,
287 potassium feldspar, and quartz in garnet are interpreted as trapped melts. In this interpretation,
288 these granitic melts approximate the initial melt composition prior to crystallization,
289 fractionation, and melt movement along the vein.

290

291 **Zircon morphology and cathodoluminescence**

292 Zircon is abundant in the host monzodiorite gneiss and in garnet reaction zones adjacent to
293 trondhjemite veins. Zircon in the host rock are 100 to 300 μm rounded, anhedral, and embayed
294 grains that are characterized by sector, patchy, and locally faint oscillatory zoning (Figs. 3 & 4).
295 Host zircon grains lack identifiable outer zones (i.e., rims) that can be readily analyzed with the
296 laser or ion beam. Zircon in the garnet reaction zone are 100 to 300 μm and vary from subhedral

297 prismatic to anhedral with numerous embayments (Figs. 3 & 4). The CL images show patchy
298 zoning, luminescent rims (Fig. 3), and a lack of coherent oscillatory or sector zoning. A few
299 garnet reaction zone zircon have identifiable outer zones from later growth (Fig. 3). These
300 narrow rims were targeted with the SHRIMP-RG ion beam.

301

302 **Zircon U-Pb CA-ID-TIMS ages**

303 Five zircon grains from the garnet reaction zone and 5 zircon grains from the host pluton
304 were analyzed by CA-ID-TIMS (Table 1; Fig. 4). The analyses from both samples display
305 (geologic) scatter in excess of analytical uncertainty and do not define single age populations.

306 Zircon from the host orthogneiss (09NZ22b) range in $^{206}\text{Pb}/^{238}\text{U}$ age from 118.30 ± 0.13 to
307 116.70 ± 0.12 Ma. The garnet reaction zone zircon (09NZ22a) range in $^{206}\text{Pb}/^{238}\text{U}$ age from
308 117.65 ± 0.25 to 115.70 ± 0.18 Ma. The ca. 118.3 to 116.7 Ma ages reported here overlap within
309 uncertainty with the calculated weighted mean $^{206}\text{Pb}/^{238}\text{U}$ date of the younger zircon populations
310 (117.5 ± 1.0 Ma) for the Malaspina Pluton at First Arm based on SHRIMP-RG U-Pb
311 geochronology (Schwartz et al., 2017), and are consistent with an ID-TIMS age (multi-grain
312 zircon) of 116.6 ± 1.2 Ma from Wet Jacket Arm (Fig. 1) (Mattinson et al., 1986; Tulloch and
313 Kimbrough, 2003).

314

315 **Zircon U-Pb SHRIMP-RG ages**

316 Fifteen zircon grains from the garnet reaction zone sample 09NZ22a and 14 zircon grains
317 from the host rock sample 09NZ22b were analyzed using the SHRIMP-RG (Table 2). Individual
318 $^{206}\text{Pb}/^{238}\text{U}$ ages for these samples range from 121.4 ± 2.0 to 109.8 ± 1.8 Ma. CL images do not
319 indicate distinctive zircon cores; however, narrow rims were identified on a few garnet reaction

320 zones grains (Fig. 3). Three zircon rims targeted via CL images (Fig. 3) yielded $^{206}\text{Pb}/^{238}\text{U}$ ages
321 of 112.3 ± 2.4 (GRZ-4.2), 117.4 ± 2.6 and 121.4 ± 2.0 Ma (GRZ-6.1): together these 3 ages are
322 indistinguishable from the overall age population. However, a single pair of garnet reaction zone
323 analyses (Fig. 3, analyses 4.1 & 4.2) yield a statistically significant and logical age progressive
324 core (118.3 ± 2.7) and rim (112.3 ± 2.4) ages. Young rims were either absent from the host
325 orthogneiss zircon or too narrow for the ion beam spot size to be analyzed (Fig. 3). However, the
326 range of ages for these host zircon (109.8 to 120.6) is indistinguishable from the range of ages
327 (109.8 to 121.4) for garnet reaction zone zircon.

328 The garnet reaction zone SHRIMP-RG zircon ages are over-dispersed and the weighted mean
329 age of 117.1 ± 2.0 Ma has an MSWD of 15.5 (no ages rejected) indicating that these ages do not
330 consist of a single meaningful population. Rejection of the 6 youngest ages, which form a stair-
331 step array to lower ages, results in a weighted mean age of 119.8 ± 1.2 Ma (Fig. 5) with an
332 MSWD of 2.3. Similarly, the host SHRIMP-RG zircon ages are over-dispersed and the weighted
333 mean age of 116.0 ± 2.0 Ma has an MSWD of 9.2 (no ages rejected). Rejection of the 2 youngest
334 ages results in a weighted mean age of 117.9 ± 0.9 Ma (Fig. 5) with an MSWD of 1.3. This 117.9
335 Ma age determined for the host (09NZ22b) from Crooked Arm is indistinguishable from the
336 weighted mean for the garnet reaction zone zircon. The young zircon ages, rejected from the
337 weighted means for the host and garnet reaction zone overlap with garnet Sm-Nd ages for this
338 sample and others from the Malaspina Pluton (Stowell et al., 2014), and metamorphic zircon and
339 titanite in the region (Schwartz et al., 2016).

340

341 **Garnet ages**

342 New Sm and Nd isotope data for 0.5 to 2 mm diameter garnet grains, clinopyroxene, matrix,
343 and whole-rock from Type 1 garnet reaction zone garnet (09NZ22) define a 5-point isochron
344 with an age of 103.6 ± 2.2 Ma (Table 3 and Fig. 6). An additional single garnet aliquot combined
345 with the clinopyroxene, whole rock, and matrix, results in a 4-point isochron age of 112.1 ± 2.4
346 Ma indistinguishable from the published age of 112.8 ± 2.2 Ma (Stowell et al. 2014) for large
347 garnet in this sample (this age was recalculated as 113.1 Ma in Table 4).

348 One core and 6 rims from the ~ 11 mm Type 2 garnet grains, and 2 whole rock aliquots, were
349 analyzed for garnet Lu-Hf geochronology (Table 3). The whole rock aliquots have notably
350 dissimilar $^{176}\text{Hf}/^{177}\text{Hf}$ values, one of which falls well below the isochron for the remaining garnet
351 and rock (Fig. 6). The whole rock aliquot dissolved in a PFA vial has a dramatically lower
352 $^{176}\text{Lu}/^{177}\text{Hf}$ ratio of 0.015739 compared to the aliquot dissolved in a bomb with
353 $^{176}\text{Lu}/^{177}\text{Hf}=0.016119$. We exclude the aliquot dissolved in PFA (WR S1 – PFA) because it may
354 not have completely dissolved and inclusion of these isotope ratios produce an age ca. 124 Ma
355 which is significantly older than U-Pb zircon ages for this sample and the pluton emplacement
356 age determined from multiple samples (Schwartz et al., 2017). The remaining 8 aliquots result in
357 an age of 111.2 ± 1.2 Ma (MSWD=0.98). The whole rock isotopic compositions may have been
358 modified by partial melting and/or biased by igneous zircon that were not in equilibrium with
359 garnet. Discounting both whole rock isotope values, results in an age of 114.8 ± 3.5 Ma
360 (MSWD=0.25) for the seven garnet aliquots. Both of these younger ages overlap within
361 uncertainty of the large garnet Sm-Nd results (Table 4 and Stowell et al., 2014).

362

363 **Major and trace element compositions of zircon and garnet**

364 Trace-element concentrations were obtained for the 29 zircon spots that were analyzed
365 simultaneously with U and Pb isotopes using the SHRIMP-RG (Fig. 7). The major and trace
366 element zoning in Type 1 and 2 garnet were characterized with lines of wavelength dispersive
367 analyses point analyses (Fig. 8). In addition, new laser ablation inductively coupled mass
368 spectrometer (LA-ICPMS) trace element data are presented for small garnet grains and a subset
369 of analyses reported in Stowell et al. (2014) for ~ 1 cm garnet grains are presented here.

370 Zircon from the host and garnet reaction zone are distinguished by contrasting trace-element
371 concentrations and magma evolution trends (Fig. 7a-h). For example, host zircon have both
372 higher average and a more extended range in Hf concentrations (Fig. 7a-f) than the garnet
373 reaction zone zircon. We observe no apparent correlation between Hf (ppm) and SHRIMP-RG
374 age, though large errors on individual spots (3-4 m.y., 2 σ) preclude the use of SHRIMP-RG data
375 for interpreting fine-scale details of magma evolution (inset Fig 7a). Garnet reaction zone zircon
376 also have lower overall middle and heavy REE concentrations compared to host zircon and show
377 little to no increase in REE concentrations with increasing Hf (ppm) and magma differentiation
378 (Fig. 7a-c). In contrast, host zircons show a strong increase in middle and heavy REE
379 concentrations during differentiation (Fig. 7a-c, g). Neither garnet reaction zone nor host zircon
380 show strong depletion in HREEs in chondrite-normalized REE abundance plots (Fig. 7h).

381 All of the zircon grains have positive Ce anomalies and small negative Eu anomalies;
382 however, host and garnet reaction zone zircon show distinct magmatic trends in Ce/Ce* and
383 Eu/Eu*. The contrasting initial Ce/Ce* values shown in Fig. 7d suggest different feldspar
384 fractionation or initial magmatic oxidation states (Trail, 2012). In addition, garnet reaction zone
385 zircon have less pronounced Eu/Eu*, a measure of the magnitude of the Eu anomaly, compared
386 to host zircons (Fig. 7e). The latter is consistent with the more extended range in Hf (ppm).

387 Zircon in the garnet reaction zone and host also show increasing Th/U with differentiation, but
388 the trends are distinct (Fig. 7f,g). Initial Th/U values converge at Th/U = 0.4, and then show
389 contrasting trends. Thus, although the cross-cutting relations and garnet ages indicate that the
390 garnet reaction zone and veins are younger, the unique trace element characteristics and trends
391 observed in the garnet reaction zone zircon indicate that they are not logically interpreted as late
392 products of a crystallization trend in a single simple magma, and the two samples cannot be
393 related by simple partial melting or fractionation processes.

394 The Ti content of zircon (SHRIMP-RG) from host and garnet reaction zone in 09NZ22
395 ranges from 13 to 49 ppm. These Ti contents are used to estimate zircon growth temperatures
396 using the thermometer of Ferry and Watson (2007), assuming activities of 0.8 for Si and 0.7 for
397 Ti, and the pressure correction described in Ferris et al. (2008). These activities are reasonable
398 for the host rock because it does not contain quartz and rutile and these values result in
399 calculated temperatures that match those estimated for amphibole crystallization in the
400 Malaspina Pluton (Carty et al. 2020). Although quartz occurs as small inclusions within Type 2
401 selvage garnet in the garnet reaction zone and is predicted to be stable near the solidus (Stowell
402 et al., 2014). The activity for Ti was likely to have been less than that of saturation based on the
403 general lack of rutile in in the matrix of host and garnet reaction zone samples. However, rutile
404 inclusions in garnet and the prediction of rutile stability in pseudosections (Stowell et al. 2014)
405 indicate that Ti activity was higher at least during the latter part of metamorphism. Although
406 some zircon may have grown and/or equilibrated during metamorphism, most zircon ages and
407 chemical compositions are compatible with growth during initial crystallization of the pluton, so
408 we utilize the activities compatible with initial igneous crystallization. Uncertainties in the Ti-in-
409 zircon temperatures are likely to be ca. 60°C as given by Ferry and Watson (2007) because the

410 activities of SiO₂ and TiO₂ are reasonably well constrained for the Malaspina Pluton samples.
411 The Ti in zircon temperature estimates range from 980°C down to 822°C (Table 2); however, the
412 lowest T estimates cannot be clearly correlated with zircon rims that have obvious CL
413 overgrowths. This range in temperature extends from above to slightly below those predicted
414 from garnet compositions (Stowell et al., 2014). Temperatures calculated from Ti-in-zircon were
415 plotted with the corresponding U-Pb ages for each grain (Fig. 9). Results show two scattered
416 trends toward lower temperature estimates with younger ages.

417 Large, ~ 10 mm garnet from Crooked Arm display complex zoning in trace elements
418 (Stowell et al., 2014). These Type 2 garnet grains from the vein selvage have concentric
419 oscillatory zoning in the heavy REE and little or no zoning in the light REE. The oscillations in
420 heavy REE are superposed on broad decreases in concentrations from core to rim (Fig. 8).
421 Samarium is weakly zoned with small-scale oscillations and a general decrease from core to rim.
422 Chondrite-normalized REE patterns have steep positive slopes from La to Eu and near-horizontal
423 HREE segments (Fig. 8). Similarly to the zircon, there is no clear evidence for equilibrium
424 between the ~ 10 mm garnet grains and zircon. Large garnet have low-amplitude oscillations in
425 Hf concentrations. Small, Type 1 garnet grains from the garnet reaction zone in 09NZ22 have
426 relatively simple zoning (Fig. 8). These grains have no systematic zoning in Nd, although a few
427 spurious points near the rim of garnet suggest possible Nd variation or Nd-bearing inclusions. In
428 contrast, Sm, Yb, and Lu show significant zoning with higher values in the cores of grains.
429 Hafnium concentrations are just above detection limits and show broad decreases from core to
430 rim (Fig. 8c).

431

432

DISCUSSION

433 **Zircon growth, Pb-loss and re-equilibration**

434 Prior studies have documented that zircon U-Pb ages and zircon trace-element compositions
435 can track crystallization, differentiation, and incremental emplacement of magmas (e.g.,
436 Coleman et al, 2004; Samperton et al., 2015). Many of these examples use zircon U-Pb data to
437 show that intermediate to silica-rich plutons comprise numerous intrusive pulses. In the case of
438 the Malaspina Pluton, our CA-ID-TIMS zircon ages are interpreted to reflect igneous
439 crystallization over ca. 2.6 m.y. and this range in age may in part reflect pulses of intrusion. The
440 stair-step array of younger SHRIMP-RG zircon ages from 116 to 110 Ma overlap with the 113
441 Ma age of peak granulite metamorphism and partial melting from garnet ages (Fig. 10). We
442 interpret these arrays of younger ages to reflect metamorphic zircon growth or recrystallization.
443 Garnet and some of the zircon grain segments with younger ages may have grown
444 simultaneously. Chondrite-normalized REE plots show moderate positive slopes for HREE in
445 zircon and flat slopes in garnet similar to those observed in these minerals from other migmatites
446 (e.g., Rubatto, 2002). These patterns support the growth of garnet with zircon present or
447 synchronous with late zircon that is supported by their overlapping isotopic ages.

448 The zircons from host orthogneiss and garnet granulite reaction zone have complex
449 morphologies and CL responses which illustrate distinct and contrasting textural characteristics
450 (Fig. 3). In addition, the two U-Pb datasets presented here for treated (CA-TIMS) and untreated
451 (SHRIMP-RG) zircon have significant ranges in dates and trace-element concentrations. We
452 utilize zircon ages, and trace-element compositions to construct a model for multiple batchwise
453 igneous intrusions and subsequent metamorphism. The ages and trace elements allow us to
454 estimate a minimum duration for intrusion, cooling rates for the Malaspina Pluton, and the time
455 between intrusion and garnet granulite metamorphism.

456 We consider three end-member alternatives to explain the observed zircon ages, lithologic
457 variations, and textural relationships (Fig. 11). All three of these scenarios could include multiple
458 zircon growth episodes and minor Pb-loss during garnet granulite metamorphism.

459 In the first scenario, the garnet reaction zones and veins formed during metamorphism and
460 partial melting of homogenous Malaspina Pluton host. The garnet reaction zone was near
461 identical in igneous mineralogy to the host rock and subsequently recrystallized into garnet +
462 clinopyroxene + partial melt with local melt migration into the adjacent trondhjemite veins.
463 These veins, which are low in potassium and include very little potassium feldspar, are modified
464 partial-melt compositions and evolved due to fractional crystallization and movement of melt out
465 of the local melt production zones. Initial zircon growth occurred during crystallization of
466 magma in the pluton between 118 and 116 Ma. This was followed by possible narrow zircon rim
467 growth (e.g., GRZ-4.2 at 112.3 ± 2.4), local zircon resorption, and possible Pb-loss from zircon
468 during metamorphism and partial melting from 115 to 111 Ma. In this scenario, melts and fluids
469 would be most likely to promote metamorphic zircon growth and modification within the garnet
470 reaction zone. Younger zircon growth and re-equilibration, partial resorption of pre-existing
471 zircon would be spatially restricted depending on fluid and melt availability. Early magmatic
472 zircon trace-element compositions would be relatively uniform due to the initial homogeneous
473 rock in what is now the host and garnet reaction zone. The two distinct Th-U trends (Fig. 7d)
474 reflect the separate evolution of the host Malaspina Pluton and the partial melt which migrated
475 toward and into the vein. Th/U versus Hf zircon groups (Fig. 7e) reflect crystallization of the
476 primary Malaspina Pluton magma and later partial melting.

477 In the second scenario, the garnet reaction zone formed from externally derived melt that was
478 injected into fractures forming veins within a relatively homogeneous host pluton. Some of this

479 melt then percolated into the adjacent host and this was accompanied by recrystallization of the
480 host to make the garnet + clinopyroxene + plagioclase-rich assemblage characteristic of the
481 garnet reaction zone. As interpreted for the first scenario, zircon first grew during crystallization
482 of the Malaspina Pluton between 118 and 116 Ma, followed by limited zircon growth (e.g.,
483 GRZ-4.2 at 112.3 ± 2.4 Ma) and modification during intrusion of the externally derived magma.
484 Zircon in the garnet reaction zone would be a combination of relict grains (partly resorbed with
485 possible Pb-loss) and new grains crystallizing from melt injection into the leucocratic veins and
486 adjacent host forming the garnet reaction zone. Zircon trace-element compositions would be
487 distinct with an initial pluton population and a secondary magma population related to magma in
488 the vein. The two distinct Th/U trends (Fig. 7d) reflect the separate evolution of the host
489 Malaspina Pluton and the younger melt injected into the vein. Th/U versus Hf zircon groups (Fig.
490 7e) reflect crystallization of the primary Malaspina Pluton magma and later magma. Overlap
491 between the compositional groups reflects physical mixing and overgrowths.

492 In the third scenario, the garnet reaction zones and veins formed during metamorphism of
493 initially heterogeneous Malaspina Pluton. The garnet reaction zone had a distinct composition
494 from the rock that was sampled as host. Although variations in the primary pluton mineralogy
495 and composition are masked by LS deformation fabrics (Fig. 2b), igneous layering and/or dikes
496 are common along Crooked Arm (Fig. 2a) and may have been present at the 09NZ22 sample
497 location. Primary lithologic variation could be related to cryptic compositional layering, perhaps
498 leading to significant variation in hydrous phases and solidus temperature. In this scenario, the
499 garnet reaction zone formed from recrystallization and partial melting of a compositional domain
500 in the pluton which differed slightly from the host sample. Melting was more prevalent in the
501 garnet reaction zone than in the host due to the initial bulk compositions. Similar to the first

502 scenario, zircon grew during initial pluton crystallization between ca. 118 and 116 Ma and the
503 two distinct Th-U trends (Fig. 7d) developed at this time. These trends reflect the different rock
504 compositions in the host and garnet reaction zone. The igneous zircon was later locally modified
505 and overgrown (e.g., GRZ-4.2 at 112.3 ± 2.4) during partial melting between 115 and 111 Ma.
506 The youngest SHRIMP-RG ages reflect these processes, but the two distinct Th-U trends and
507 Th/U versus Hf zircon groups (Fig. 7d and 7e) reflect the separate evolution of two primary host
508 Malaspina Pluton magmas.

509 In all of these three scenarios, the youngest melts in the garnet reaction zone would have
510 reacted with minerals as melt fluxed through the solid matrix (e.g., Stuart et al., 2018). This
511 reactive transport at temperatures in excess of 800°C would likely lead to complete equilibration
512 of some phases, but not others. For example, zircon SHRIMP-RG age ranges, and their trace-
513 element concentrations and compositional trends (Fig. 7) are compatible with progressive
514 changes occurring during growth in equilibrium with melts. The distinct clustering of zircon
515 compositions with minor overlap between those in the host and garnet reaction zone best fit the
516 third scenario. Therefore, we tentatively infer that the zircon data reflect two distinct igneous
517 crystallization histories for the two samples from Crooked Arm and later partial modification
518 during granulite facies metamorphism. However, the likelihood of significant compositional
519 changes during reactive flux of melt through the garnet reaction zone remains a possible
520 explanation for the observations.

521 The ages, compositions, and CL images for zircon presented here indicate the difficulty in
522 using these observations for interpreting rock history. There are subtle differences in the
523 morphology and CL images between zircon in the garnet reaction zone versus the host. Garnet
524 reaction zone zircon are anhedral with numerous embayments and the CL images indicate a lack

525 of coherent oscillatory zoning. In contrast, the host zircon are mostly rounded in form and have
526 both sector and oscillatory CL zoning. However, these differences do not correlate clearly with
527 age. Much of the soccer ball zircon with diffuse oscillatory zoning in the Malaspina Pluton has
528 been interpreted as igneous (e.g., Stowell et al. 2014; Schwartz et al. 2017) and our data
529 generally support this interpretation. The largely soccer ball zircon in the host have SHRIMP-RG
530 ages that range from the oldest to the youngest values observed in the Malaspina Pluton along
531 Crooked Arm. Our data indicate that these oscillatory zoned zircon may not have been closed to
532 U and Pb because individual spot ages from areas with the same type of CL response have ages
533 that vary by more than 5 m.y.

534 Trace-element concentrations and ratios in co-existing minerals are a powerful tool for
535 evaluating equilibrium (e.g., Rubatto 2002). In some cases, trace-element data for a single
536 mineral provide important information about equilibrium of a mineral with phases not currently
537 found in the sample (e.g., Wood et al. 2013; Rubatto et al. 2007). In addition, trivalent and
538 quadrivalent ion ratios in zircon provide constraints on igneous fractionation and possible
539 diffusion. Thorium/uranium ratios have been considered a tool for discriminating between
540 igneous and metamorphic zircon (e.g., Rubatto, 2002). Many metamorphic zircon have Th/U
541 ratios <0.1 due to very low availability of Th and or partitioning into other phases during
542 metamorphism. This is at best imperfect, because as summarized by Harley et al. (2007), there
543 are abundant examples of zircon that cannot be correctly classified with this discrimination ratio.
544 However, Th/U ratios may reflect crystallization and evolution of a magma. In the migmatite
545 from Crooked Arm, distinct trends in Th vs. U and Th/U versus age (Fig. 7) are compatible with
546 differing and distinct primary magmas in these rocks. In the garnet reaction zone, partial melting

547 and possible melt injection resulted in a more silica-rich composition than bulk Malaspina
548 magmas and we infer that these processes failed to erase the distinct zircon signatures.

549 Assuming that all of the CA-TIMS zircon ages reflect igneous crystallization, then they
550 indicate the minimum duration of Malaspina intrusion and crystallization. These zircon age
551 ranges are from 118.4 to 116.6 Ma with a duration of 1.8 m.y., and 117.9 to 115.5 Ma with a
552 duration of 2.4 m.y. for the host and garnet reaction zone, respectively. Because the age ranges
553 only overlap in part, the age range for both data sets is from 118.4 to 115.5 Ma and the duration
554 is 2.9 m.y. for the Malaspina Pluton along this part of Crooked Arm.

555

556 **Garnet ages as a reflection of peak and post peak metamorphism**

557 Large garnet have low-amplitude major element zoning with bell-shaped gradients in mole
558 fraction of spessartine (Sps) and pronounced variations in trace element concentrations (Fig. 8).
559 The sharp concentration gradients in REE are defined by multiple analyses for each concentric
560 band (Fig. 8) and are interpreted as growth zoning (Stowell et al. 2014). Samarium, Nd, and Lu
561 concentrations vary by ~ 1.5 ppm, and Yb by >3 ppm. These major and trace element variations
562 suggest that there diffusion of major elements may have been significant, but that there was little
563 or no significant diffusion of REE within the large garnet grains. Closure temperatures in garnet
564 are useful for evaluating cooling histories (e.g., Dodson, 1973; Ganguly et al., 1998; Ganguly
565 and Tirone, 1999) and we adopt the simple closure temperature formulation of Dodson (1973)
566 because the garnet reaction zone grains are interpreted to have been completely modified by
567 diffusion, the surrounding melt could have approximated a homogenous matrix, and finally for
568 slow cooling and small grain sizes the closure temperature models converge (Ganguly et al.,
569 1998; Ganguly and Tirone, 1999). Closure temperatures for Nd diffusion were estimated using

570 the slow diffusion formulation of Bloch et al. (2020), appropriate for high pressure, and
571 compared to that of Carlson (2012). The results (Table 4) indicate that the largest grains with 5-6
572 mm radius would have closure temperatures of 870 to 1090°C with cooling rates of 15 to
573 25°C/m.y. Therefore, regardless of formulation the Sm-Nd ages for large garnet should
574 approximate the timing of peak metamorphism. The Lu-Hf age of 115 Ma is tentatively preferred
575 over ages calculated with surrounding minerals because Lu-Hf ages should be biased toward
576 core growth (e.g., Lapen, 2003) and significant diffusion of Lu and Hf would require higher
577 temperatures than Sm and Nd (e.g., Carlson, 2012; Bloch et al., 2020), resulting in older Lu-Hf
578 ages. Trace element zoning in garnet are compatible with little or diffusion of REE and Hf in
579 large garnet (Fig. 8) and the two isotopic systems result in indistinguishable ages However,
580 the 115 Lu-Hf age uncertainty of 4 m.y. is too large for a definitive interpretation of any age
581 difference between the two isotopic systems.

582 Small garnet grains have little zoning in major elements, lack high spessartine cores, and
583 show pyrope, and increased grossular close to the rims (Fig. 8a). These small-scale trends in
584 major element concentrations mimic those found in the outermost rims of the large grains. The
585 trace element concentrations in small garnet show zigzag patterns anchored by single analyses
586 (Fig. 8d). The cause of this variation which exceeds analytical uncertainty is unknown; however,
587 it may result from inclusions. Ignoring these oscillations, Sm and Nd show little or no variation,
588 and Yb, Hf, and Lu show low amplitude variation with high core and lower rim concentrations.
589 Based on the compositional zoning, the 103.6 Ma garnet Sm-Nd age for small garnet reaction
590 zone grains could reflect late garnet growth or isotopic re-equilibration during cooling. We infer
591 that these small grains exchanged REE with clinopyroxene and or apatite both of which are
592 intergrown with garnet in the garnet reaction zone. The Nd closure temperatures for garnet based

593 on Bloch et al. (2020) are 690, 700, and 710°C for 0.5 mm radius and cooling rates of -15, -20,
594 and -25°C /m.y., respectively (Table 4). The garnet textures (Fig. 2) are most compatible with
595 synchronous growth of Type 1 and 2 garnet during vein emplacement; therefore, we infer that
596 Type 2 garnet was significantly modified by diffusion and use the closure temperature to
597 calculate cooling rates below.

598

599 **Cooling rates determined from zircon and garnet**

600 The most comprehensive high-precision, SHRIMP-RG zircon age results for the Malaspina
601 Pluton (Schwartz et al. 2017; and herein) indicate that most of the magma intruded ca. 118-116
602 Ma. Initial cooling occurred in the lower crust prior to significant extension at ca. 108-106 Ma
603 (Stowell et al. 2014; Schwartz et al. 2016; Klepeis et al. 2016). Garnet Sm-Nd ages from across
604 the Misty and Malaspina plutons indicate that garnet granulite metamorphism of the plutons was
605 at 111.7 ± 1.0 Ma, ca. 5 m.y. after intrusion (Stowell et al., 2014; 2017). Either the pluton cooled
606 slowly and remained hot through garnet growth or initial cooling was followed by reheating to ~
607 920°C triggering local garnet growth. In the first scenario, a local trigger for partial melting and
608 garnet growth is required. This could have been volatile flux with or without externally derived
609 melt (Clarke et al., 2005). However, abundant Type 3 isolated garnet grains with leucosome
610 halos, variably distributed in the Malaspina Pluton, indicate that local garnet growth was
611 independent of external fluids and magma veins. Therefore, we infer that much or all garnet
612 growth resulted from post emplacement heating of the heterogeneous pluton.

613 Metamorphic temperature estimates, the age of large garnet, and the Nd closure temperatures
614 for small garnet (Table 4) provide a means for calculating the cooling rate. Choosing a radius of
615 0.5 mm for small garnet, iterative calculation of the cooling rate and the garnet closure

616 temperature results in best estimates of $\sim 20^{\circ}\text{C}/\text{m.y.}$ and $\sim 700^{\circ}\text{C}$ (Fig. 9). This cooling rate is
617 similar to the approximate slope for the array of Ti in zircon temperatures and corresponding U-
618 Pb ages (Fig. 9). The cooling rate estimated here is approximately half the $\sim 50^{\circ}\text{C}/\text{m.y.}$ estimated
619 from zircon and titanite ages in Flowers et al. (2005) and higher than estimates of $8\text{-}14^{\circ}\text{C m.y.}$ in
620 Schwartz et al. (2016).

621 IMPLICATIONS

622 The identification of igneous and metamorphic zircon grains, overgrowths of metamorphic
623 zircon on prior crystals, zircon affected by Pb loss cannot always be made from CL images and
624 crystal morphology in migmatitic granulite facies rocks. This observation is supported by several
625 datasets: a) the large range of ages for each zircon morphology and CL type; b) the near
626 complete lack of clearly igneous prismatic grain shapes in both host and garnet reaction zone
627 lithologies; c) the significant population of zircon U-Pb ages that match ages for igneous
628 crystallization determined for Malaspina Pluton samples with primary igneous textures; and d)
629 the 11-14 m.y. range (considering uncertainties) of concordant SHRIMP-RG U-Pb ages
630 determined from targeted CL spots. Finally, the overlap of younger zircon U-Pb ages with Sm-
631 Nd and Lu-Hf ages for metamorphic garnet growth.

632 Assigning SHRIMP-RG U-Pb zircon ages to intrusion versus later metamorphism and partial
633 melting is difficult in our dataset due to the large range in dates from >118 to <110 Ma. In
634 addition, the two core rim pairs include one with normal and one with reverse age zoning.
635 Therefore, we conclude that multiple isotope data sets from several samples are essential for
636 unraveling the igneous and metamorphic history of migmatites.

637 Unraveling the history of this lower crustal migmatite is complicated by inferred
638 premetamorphic igneous complexity. The range in CA-TIMS zircon ages and distinct groups in

639 Sm, Yb, Ce, and Eu values versus Hf (Figs. 7a, 7b) are compatible with more than one magma.
640 This is supported by field evidence for incremental construction of the Malaspina Pluton by
641 sheeted intrusion into a crystal mush zone (Klepeis et al., 2016). The zircon dates and
642 compositions are compatible with two distinct magmas that crystallized between 118 and 116
643 Ma that underwent different fractional crystallization trends evident in the “host” and garnet
644 reaction zone samples. Deformation which produced the LS fabric has obscured textural
645 evidence for the contact between these intrusions and some magma mixing is possible. In
646 addition, the garnet reaction zone leucosome may include melt injected into the partially melted
647 garnet reaction zone from the vein.

648 Intracrystalline diffusion of trace elements was insignificant in large garnet grains. The
649 oscillatory and bell-shaped trace element zoning in garnet indicates that diffusion has played a
650 limited role in garnet trace element distributions. In addition, calculated closure temperatures
651 indicate that modification of REE by diffusion could not have affected the interiors of these
652 crystals. We conclude that large euhedral garnet can preserve growth ages recorded by both Lu-
653 Hf and Sm-Nd systems with uncertainties of ca. 2 m.y.

654 Zircon and garnet ages indicate a brief interval between pluton emplacement and garnet
655 growth (Fig. 10). The CA-TIMS U-Pb zircon ages of 118.3-115.7 and garnet ages of ca. 113 Ma
656 require 2.7 to 5.3 m.y. between pluton crystallization and granulite metamorphism. This
657 temperature increase shortly after intrusion is compatible with a magmatic pulse. No magmas of
658 this age are known in the Western Fiordland Orthogneiss and the granulite event is tentatively
659 attributed to magmatic underplating.

660 Zircon SHRIMP-RG ages of ca. 121 and 115 Ma anchor the high temperature ends of two Ti
661 in zircon temperature – age clusters which could represent distinct crystallization trends. Garnet

662 Sm-Nd growth and cooling ages overlap with younger of these clusters indicating a cooling rate
663 of $\sim 20^{\circ}\text{C}/\text{m.y.}$ from 920 to about 700°C after the peak of granulite metamorphism. Cooling rates
664 for the lower crust of a continental magmatic arc are difficult to obtain due to limited exposure
665 and geological complexity. Mid- to lower-crustal rocks of the Coast Mountains batholith in
666 Canada cooled 2 to $11^{\circ}\text{C}/\text{m.y.}$ after granulite facies metamorphism at pressures of ~ 10 kbar
667 (Hollister, 1982; Rusmore et al., 2005). The data for lower crustal rocks in the Coast Mountains
668 and Fiordland are taken to indicate that the lower crust of continental magmatic arcs may cool at
669 rates $<25^{\circ}\text{C}/\text{m.y.}$

670 The mid- to lower-crustal emplacement of the Malaspina Pluton and lack of supracrustal
671 rocks with a metamorphic history shared with these rocks preclude construction of a significant
672 prograde path. However, the $\sim 20^{\circ}\text{C}/\text{m.y.}$ cooling rate for a single location in the Malaspina
673 Pluton provides a robust estimate for cooling from ~ 920 to 700°C . Additional data are needed to
674 evaluate the spatial extent and variation of cooling rates across the lower crustal rocks in
675 Fiordland. This new cooling rate for the Crooked Arm outcrop is far slower than estimates for
676 cooling of granulite in the U.S.A. Adirondacks (Storm and Spear, 2005) or initial cooling of
677 Dora Maira Massif in the Western Alps (Engi et al., 2017), but similar to estimates for cooling of
678 ultrahigh temperature granulite from the Saxon Granulite Massif in Germany (Romer and
679 Rötzler, 2001). Both of these examples are constructed from composite P-T-t paths and/or
680 diffusion models which include data input from multiple samples. Large datasets of
681 comprehensive linked P-T-t data for individual outcrops are needed to better understand tectonic
682 histories in lower crustal rocks in Fiordland and elsewhere.

683

684

ACKNOWLEDGMENTS

685 The authors thank Jeff Vervoort at Washington State University and Kenneth Horkley for
686 assistance with garnet Lu-Hf geochronology, Karen Odom Parker at the University of Alabama
687 for assistance in establishing the UA RadIs lab, Alan Koenig (United States Geological Survey)
688 and Zahn Peng (California State University at Northridge) for help obtaining trace-element
689 garnet data, and Matthew Coble for assistance with the SHRIMP-RG data. This work could not
690 have been completed without National Science Foundation grant EAR 1119039 which supported
691 establishment of the UA RadIs laboratory. SHRIMP-RG zircon dating was supported by NSF
692 EAR-1352021.

693

694 REFERENCES CITED

- 695 Allibone, A.H., Jongens, R., Scott, J.M., Tulloch, A.J., Turnbull, I.M., Cooper, A.F., Powell, N.G.,
696 Ladley, E.B., King, R.P. and Rattenbury, M.S. (2009) Plutonic rocks of the Median Batholith in
697 eastern and central Fiordland, New Zealand: Field relations, geochemistry, correlation, and
698 nomenclature. *New Zealand Journal of Geology and Geophysics*, 52, 01-148.
- 699 Baxter E.F., Caddick, M.J., and Dragovic, B. (2017) Garnet: a rock forming mineral petrochronometer,
700 *Reviews in Mineralogy and Geochemistry*. 83, 469-533.
- 701 Baxter E.F. and Scherer, E.E. (2013) Garnet: timekeeper of tectonometamorphic processes. *Elements*, 9, 6,
702 433-438.
- 703 Begemann, F., Ludwig, K.R., Lugmair, G.W., Min, K., Nyquist, L.E., Patchett, P. J., Renne, P.R., Shih,
704 C.-Y., Villa, I.M., and Walker, R.J. (2001) Call for an improved set of decay constants for
705 geochronological use. *Geochimica et Cosmochimica Acta*, 65, 111-121.
- 706 Blattner, P. (1976) Replacement of hornblende by garnet in granulite facies assemblages near Milford
707 Sound, New Zealand. *Contributions to Mineralogy and Petrology*, 55, 181– 190.
- 708 Bloch, E., Ganguly J., Hervig, R., and Cheng, W. (2015) ^{176}Lu – ^{176}Hf geochronology of garnet I:

- 709 experimental determination of the diffusion kinetics of Lu³⁺ and Hf⁴⁺ in garnet, closure temperatures
710 and geochronological implications. *Contributions to Mineralogy and Petrology*, 169, 12.
- 711 Bloch, E.M., Jollands, M.C., Devoir, A., Bouvier, A-S., Ibañez-Mejia, M., and Baumgartner, L.P. (2020)
712 Multispecies diffusion of yttrium, rare earth elements and hafnium in garnet. *Journal of Petrology*,
713 egaa055, <https://doi.org/10.1093/petrology/egaa055>
- 714 Bradshaw, J.Y. (1989) Origin and metamorphic history of an Early Cretaceous polybaric granulite terrain,
715 Fiordland, southwest New Zealand. *Contributions to Mineralogy and Petrology*, 103, 346–360.
- 716 Carlson, W. (2012) Rates and mechanism of Y, REE, and Cr diffusion in garnet. *American Mineralogist*,
717 97, 1598–1618.
- 718 Carty, K., Schwartz, J.J., and Barnes, C.G. (2019) Testing the “MASH” hypothesis an investigation of
719 magma chamber geometry and interconnectivity in the lower crust of a continental arc, Fiordland,
720 New Zealand. *Geological Society of America Abstracts with Programs*, 51, 5, doi:
721 10.1130/abs/2019AM-340018
- 722 Cheng, H., King, R.L., Nakamura, E., Vervoort, J.D., and Zhou, Z. (2008) Coupled Lu-Hf and Sm-Nd
723 geochronology constrains garnet growth in ultra-high-pressure eclogites from the Dabie orogen.
724 *Journal of Metamorphic Geology*, 26, 741–758.
- 725 Cherniak, D.J., Hancher J.M., and Watson E.B. (1997a) Diffusion of tetravalent cations in zircon.
726 *Contributions to Mineralogy and Petrology*, 127, 383-390.
- 727 Cherniak, D.J., Hancher J.M., and Watson E.B. (1997b) Rare earth diffusion in zircon. *Chemical Geology*
728 134, 289-301.
- 729 Clarke, G.L., Daczko, N., Klepeis, K.A., and Rushmer, T. (2005) Roles for fluid and/or melt advection in
730 forming high-P mafic migmatites, Fiordland, New Zealand. *Journal of Metamorphic Geology*, 23,
731 557-567.
- 732 Coble, MA., Vazquez, J.A., Barth, A.P., Wooden, J., Burns, D., Kylander-Clark, A., Jackson, S., and
733 Vennari, C.E. (2018) Trace Element Characterization of MAD-559 Zircon Reference Material for Ion
734 Microprobe Analysis. *Geostandards and Geoanalytical Research*, 42, 481-497

- 735 Coleman, D.S., Gray, W., and Glazner, A. F. (2004) Rethinking the emplacement and evolution of zoned
736 plutons: geochronologic evidence for incremental assembly of the Tuolumne Intrusive Suite,
737 California. *Geology*, 32 5, 433-436, doi: 10.1130/G20220.1.
- 738 Daczko, N.R. and Halpin, J.A. (2009) Evidence for melt migration enhancing recrystallization of
739 metastable assemblages in mafic lower crust, Fiordland, New Zealand. *Journal of Metamorphic*
740 *Geology*, 27, 167-185.
- 741 Daczko, N., Piazzolo, S., Meek, U., Stuart, C.A., and Elliott, V. (2016) Hornblendite delineates zones of
742 mass transfer through the lower crust. *Scientific Reports*, 6, <https://doi.org/10.1038/srep31369>.
- 743 Decker, M., Schwartz, J.J., Stowell, H.H., Klepeis, K., Tulloch, A., Kiajima, A., Valley, J.W., and
744 Kylander-Clark, A. (2017) Slab-Triggered Arc Flare-up in the Cretaceous Median Batholith and the
745 Growth of Lower Arc Crust, Fiordland, New Zealand. *Journal of Petrology*, 58, 6, 1145-1172.
- 746 Dodson, M.H. (1973) Closure temperatures in cooling geochronological and petrological systems.
747 *Contributions to Mineralogy and Petrology*, 40, 259-274.
- 748 Donovan, J. (2010) Probe for EPMA, Eugene, Oregon, Probe Software, [https://www.probesoftware.com](https://www.probesoftware.com/index.html)
749 [/index.html](https://www.probesoftware.com/index.html) (accessed June 2019).
- 750 Ducea, M.N., Saleeby, J.B., and Bergantz, G. (2015) The architecture, chemistry, and evolution of
751 continental magmatic arcs. *Annual Review of Earth and Planetary Sciences*, 43, 1, 299-331.
- 752 Eddy, M.P., Ibañez-Mejia, M., Burgess, S.,D., Coble, M.A., Cordani, U.G., DesOrmeau, J., Gehrels,
753 G.E., Li, X., MacLennan, S., Pecha, M., Sato, K., Schoene, B., Valencia, V.A., Vervoort, J.D., and
754 Wang, T. (2018) GHR1 Zircon – a new Eocene natural reference material for in situ U-Pb
755 geochronology and Hf isotopic analysis of zircon. *Geostandards and Geoanalytical Research*, doi:
756 [10.1111/ggr.12246](https://doi.org/10.1111/ggr.12246).
- 757 Engi, M., Lanari, P., and Kohn, M.J. (2017) Significant ages—an introduction to petrochronology, in
758 Kohn, M.J., Engi, M., Lanari, P., eds., *Petrochronology: methods and applications*, *Reviews in*
759 *Mineralogy and Geochemistry*, 83, 1-12.

- 760 Hollister, L.S. (1982) Metamorphic evidence for rapid (2 mm/yr) uplift of a portion of the Central Gneiss
761 Complex, Coast Mountains, B.C, Canadian Mineralogist, 20, 319 – 332.
- 762 Ferriss, E.D.A. Essene, E.J., and Becker, U. (2008) Computational study of the effect of pressure on the
763 Ti-in-zircon geothermometer. European Journal of Mineralogy, 20, 745 – 755.
- 764 Ferry, J.M., and Watson, E.B. (2007) New thermodynamic models and revised calibrations for the Ti-in-
765 zircon and Zr-in-rutile thermometers. Contributions to Mineralogy and Petrology, 154, 429–437,
- 766 Ganguly, J., Tirone, M., and Hervig, R. (1998) Diffusion kinetics of samarium and neodymium in garnet
767 and a method for determining cooling rates of rocks. Science, 281, 805-807.
- 768 Ganguly, J., and Tirone, M. (1999) Closure temperature, cooling age and high temperature
769 thermochronology, in Physics and Chemistry of the Earth's Interior: crust, mantle and core. Gupta
770 A.K., Dasgupta S., eds., Indian National Science Academy-Springer (India), 89-98.
- 771 Gatewood, M.P., Dragovic, B. Stowell, H.H., Baxter, E.F., Hirsch, D.M., and Bloom, R.A. (2015)
772 Evaluating chemical equilibrium in metamorphic rocks using major element and Sm-Nd isotopic age
773 zoning in garnet, Townsend Dam, Vermont, USA. Chemical Geology, 401, 151-168.
- 774 Gibson, G.M., and Ireland, T.R. (1995) Granulite formation during continental extension in Fiordland,
775 Nature, 375, 479–482.
- 776 Gibson, G.M., McDougall, I., and Ireland, T.R. (1988) Age constraints on metamorphism and
777 development of a metamorphic core complex in Fiordland, southern New Zealand, Geology, 16, 405–
778 408.
- 779 Hacker, B.R., Mehl, L., Kelemen, P.B., Rioux, M., Behn, M.D. and Luffi, P. (2008) Reconstruction of the
780 Talkeetna intraoceanic arc of Alaska through thermobarometry. Journal of Geophysical Research, 113,
781 B03204.
- 782 Hammerli, J., Kemp, A.I.S., Shimura, T., Vervoort, J., EIMF, and Dunkley, D.J. (2018) Generation of I-
783 type granitic rocks by melting of heterogeneous lower crust. Geology,
784 <https://doi.org/10.1130/G45119.1>
- 785 Harley, S.L., Kelly, N.M., and Möller, A. (2007) Zircon behavior and the thermal histories of mountain

- 786 chains. *Elements*, 3, 25–30.
- 787 Hollis, J.A., Clarke, G.L., Klepeis, K.A., Daczko, N.R., and Ireland, T.R. (2004) The regional
788 significance of Cretaceous magmatism and metamorphism in Fiordland, New Zealand, from U-Pb
789 zircon geochronology. *Journal of Metamorphic Geology*, 22, 607–627.
- 790 Hoskin, P.W.O., and Schaltegger, U. (2003) The composition of zircon and igneous and metamorphic
791 petrogenesis. *Reviews in Mineralogy and Geochemistry*, 53, 1, 27-62.
- 792 Jagoutz, O. (2010) Construction of the granitoid crust of an island arc. Part II: a quantitative petrogenetic
793 model. *Contributions to Mineralogy and Petrology*, 160 (3), 359-381.
- 794 Kay, R.W., and Mahlburg Kay, S. (1993) Delamination and delamination magmatism. *Tectonophysics*,
795 219, 177-189.
- 796 Klepeis, K.A., Clarke, G.L., and Rushmer, T. (2003) Magma transport and coupling between deformation
797 and magmatism in the continental lithosphere. *GSA Today*, 13, 4–11.
- 798 Klepeis, K.A., Schwartz, J., Stowell, H., and Tulloch, A. (2016) Gneiss domes, vertical and horizontal
799 mass transfer, and the initiation of extension in the hot lower crustal root of a continental arc,
800 Fiordland, New Zealand. *Lithosphere*, 8, 116-140.
- 801 Lapen, T.J., Johnson, C.M., Baumgartner, L.P., Mahlen, N.J., Beard, B.L., and Amato, J.M. (2003) Burial
802 rates during prograde metamorphism of an ultra-high-pressure terrane: an example from Lago di
803 Cignana, western Alps, Italy. *Earth and Planetary Science Letters*, 215, 57-72.
- 804 Lee, CT, Cheng, X, and Horodyskyi, U. (2006) The development and refinement of continental arcs by
805 primary basaltic magmatism, garnet pyroxenite accumulation, basaltic recharge and delamination:
806 insights from the Sierra Nevada, California. *Contributions to Mineralogy and Petrology*, 151, 222–42
- 807 Ludwig, K.R. (2009) *Squid 2: A user's Manual*. Berkeley Geochronology Center Special Publication 5, 1–
808 110.
- 809 Ludwig, K.R. (2012) *User's manual for Isoplot 3.75–4.15: A geochronological toolkit for Microsoft Excel*.
810 Berkeley Geochronology Center Special Publication, 5, 74.

- 811 Lugmair, G.W., and Marti, K. (1978) Lunar initial $^{143}\text{Nd}/^{144}\text{Nd}$: differential evolution of the lunar crust
812 and mantle. *Earth and Planetary Science Letters*, 39, 349-357.
- 813 Mattinson, J.M. (2005) Zircon U–Pb chemical abrasion (“CA-TIMS”) method: Combined annealing and
814 multi-step partial dissolution analysis for improved precision and accuracy of zircon ages. *Chemical*
815 *Geology*, 220, 47-66.
- 816 Mattinson, J.M., Kimbrough, D.L., and Bradshaw, J.Y. (1986) Western Fiordland orthogneiss: Early
817 Cretaceous arc magmatism and granulite facies metamorphism, New Zealand. *Contributions to*
818 *Mineralogy and Petrology*, 92, 383-392.
- 819 McDonough, W.F., and Sun, S.S. (1995) The composition of the Earth. *Chemical Geology*, 120, 223-253.
- 820 Mezger, K., Essene, E.J., and Halliday, A.N. (1992) Closure temperatures of the Sm-Nd system in
821 metamorphic garnets. *Earth and Planetary Science Letters*, 113, 397-409.
- 822 Milan, L.A., Daczko, N.R., Clarke, G.L., and Allibone, A.H. (2016) Complexity of in-situ zircon U-Pb-
823 Hf isotope systematics during arc magma genesis at the roots of a Cretaceous arc, Fiordland, New
824 Zealand. *Lithos*, 264, 296–314.
- 825 Oliver, G.J.H. (1977) Feldspathic hornblende and garnet granulites and associated anorthosite pegmatites
826 from Doubtful Sound, Fiordland, New Zealand. *Contributions to Mineralogy and Petrology*, 65, 111–
827 121.
- 828 Oliver, G.J.H. (1980) Geology of the granulite and amphibolite facies gneisses of Doubtful Sound,
829 Fiordland, New Zealand. *New Zealand Journal of Geology and Geophysics*, 23, 27–41.
- 830 Oliver, G.J.H., Coggon, J.H. (1979) Crustal structure of Fiordland, New Zealand. *Tectonophysics*, 54,
831 253-292.
- 832 Paton, C., Hellstrom, J., Paul, B., Woodhead, J. and Hergt, J. (2011) Iolite: Freeware for the visualisation
833 and processing of mass spectrometric data, *Journal of Analytical Atomic Spectrometry*. 26(12), 2508,
834 doi:10.1039/c1ja10172b.

- 835 Ramezani, J., Schmitz, M. D., Davydov, V. I., Bowring, S. A., Snyder, W. S., and Northrup, C. J. (2007)
836 High-precision U-Pb zircon age constraints on the Carboniferous-Permian boundary in the southern
837 Urals stratotype. *Earth and Planetary Science Letters*, 256, 1-2, 244-257.
- 838 Romer, R.L., and Rötzler, J. (2001) P-T-t Evolution of ultrahigh-temperature granulites from the Saxon
839 Granulite Massif, Germany. Part II: Geochronology. *Journal of Petrology*, 42, 2015-2032.
- 840 Rubatto, D. (2002) Zircon trace element geochemistry: partitioning with garnet and link between U-Pb
841 ages and metamorphism. *Chemical Geology*, 184, 123-138.
- 842 Samperton, K.M., Schoene, B., Cottle, J.M., Keller, C.B., Crowley, J.L., and Schmitz, M.D. (2015)
843 Magma emplacement, differentiation and cooling in the middle crust: Integrated zircon
844 geochronological-geochemical constraints from the Bergell Intrusion, Central Alps. *Chemical*
845 *Geology*, 417, 322-340.
- 846 Scherer E., Münker, C., and Mezger, K. (2001) Calibration of the lutetium-hafnium clock. *Science*, 293,
847 683-687.
- 848 Schwartz, J.J., Stowell, H.H., Klepeis, K., Zamora, C., Tulloch, A., Kylander-Clark, A., Hacker, B., and
849 Coble, M. (2016) Thermochronology of extensional orogenic collapse in the deep crust, Fiordland,
850 New Zealand. *Geosphere*, 12, 3, 1-31.
- 851 Schwartz, J.J., Klepeis, K., Sadowski, J.F., Stowell, H.H., Tulloch, A., and Coble, M. (2017) The tempo of
852 continental arc construction in the Mesozoic Median Batholith, Fiordland, New Zealand. *Lithosphere*.
853 doi:10.1130/L610.1.
- 854 Smit, M., Scherer, E., and Mezger, K. (2013) Lu-Hf and Sm-Nd garnet geochronology: chronometric
855 closure and implications for dating petrological processes. *Earth and Planetary Science Letters*, 381,
856 222-233.
- 857 Smit, M., Scherer, E., and Mezger, K. (2014) Corrigendum to “Lu-Hf and Sm-Nd garnet geochronology:
858 chronometric closure and implications for dating petrological processes”. *Earth and Planetary Science*
859 *Letters*. 381, 222-233.
- 860 Söderlund, U., Patchett, P.J., Vervoort, J.D., and Isachsen, C.E. (2004) The ^{176}Lu decay constant

- 861 determined by Lu-Hf and U-Pb isotope systematics of Precambrian mafic intrusions. Earth and
862 Planetary Science Letters, 219, 311-324.
- 863 Stacey, J.S., and Kramers, J.D. (1975) Approximation of terrestrial lead isotope evolution by a two-stage
864 model. Earth and Planetary Science Letters, 26, 2, 207-221.
- 865 Stevenson, J.A., Daczko, N.R., Clarke, G.L., Pearson, N., and Klepeis, K.A. (2005) Direct observation of
866 adakite melts generated in the lower continental crust, Fiordland, New Zealand. Terra Nova 17, 73–
867 79.
- 868 Storm, L.C., and Spear, F.S. (2005) Pressure, temperature and cooling rates of granulite facies migmatitic
869 pelites from the southern Adirondack Highlands, New York. Journal of Metamorphic Geology, 23,
870 107-130.
- 871 Stowell, H.H., Bulman, G.R., Zuluaga, C.A., Tinkham, D.K., and Miller, R.B. (2007) Mid-Crustal Late
872 Cretaceous Metamorphism in the Nason Terrane, Cascades Crystalline Core, Washington, USA,
873 Implications for Tectonic Models, in Hatcher, R.D., Jr., Carlson, M.P., McBride, J.H., & Martínez
874 Catalán, J.R., eds., 4-D Framework of Continental Crust. Geological Society of America Memoir 200,
875 211-231.
- 876 Stowell, H.H., Odom Parker, K., Gatewood, M.P., Tulloch, A., and Koenig, A. (2014) Temporal links
877 between pluton emplacement, garnet granulite metamorphism, partial melting, and extensional
878 collapse in the lower crust of a Cretaceous magmatic arc, Fiordland New Zealand. Journal of
879 Metamorphic Geology, 32, 151-175.
- 880 Stowell, H.H., Schwartz, J.J., Klepeis, K., Hout, C., Tulloch, A., Koenig, A., 2017, Sm-Nd garnet ages for
881 granulite and eclogite in the Breaksea Orthogneiss and widespread granulite facies metamorphism of
882 the lower crust, Fiordland magmatic arc, New Zealand. *Lithosphere*. doi.org/10.1130/L662.1
- 883 Stowell, H.H., Tulloch, A., Zuluaga, C.A., and Koenig, A. (2010) Timing and duration of garnet granulite
884 metamorphism in magmatic arc crust, Fiordland, New Zealand. Chemical Geology, 273, 91-110.
- 885 Stuart, C.A., Meek, U., Daczko, N.R., Piazzolo, S., and Huang, J.-X., 2018. Chemical signatures of melt-
886 rock interaction in the root of a magmatic arc. Journal of Petrology, 59, 321-340.

- 887 Tanaka, T., Togashi, S., Kamioka, H., Amakawa, H., Kagami, H., Hamamoto, T., Yuhara, M., Orihashi,
888 Y., Yoneda, S., Shimizu, H., Kunimaru, T., Takahashi, K., Yanagi, T., Nakano, T., Fujimaki, H.,
889 Shinjo, R., Asahara, Y., Tanimizu, M., and Dragusanu, C. (2000) JNdi-1: a neodymium isotopic
890 reference in consistency with LaJolla neodymium. *Chemical Geology*, 168, 279–281.
- 891 Tirone, M., Ganguly, J., Dohmen, R., Langenhorst, F., Hervig, R., and Becker, H.-W. (2005) Rare earth
892 diffusion kinetics in garnet: experimental studies and applications. *Geochimica et Cosmochimica*
893 *Acta*, 69, 2385-2398.
- 894 Trail, D., Watson, E.B., and Tailby, N.D. (2012) Ce and Eu anomalies in zircon as proxies for the
895 oxidation state of magmas. *Geochimica et Cosmochimica Acta*, 97, 70-87.
- 896 Tulloch, A.J., and Kimbrough, D. (2003) Paired plutonic belts in convergent margins and the
897 development of high Sr/Y magmatism: Peninsular Ranges batholith of Baja-California and Median
898 batholith of New Zealand. *Geological Society of America Special Paper*, 374, 275–296.
- 899 Turnbull, I.M., Allibone, A.H., and Jongens, R., (compilers) (2010) *Geology of the Fiordland area, New*
900 *Zealand*. GNS Science, Lower Hutt, New Zealand, Institute of Geological and Nuclear Sciences,
901 *Geological Map 17, scale 1:250 000, 1 sheet*.
- 902 Vermeesch, P. (2018) IsoplotR: a free and open toolbox for geochronology. *Geoscience Frontiers*, 9,
903 1479-1493.
- 904 Vervoort, J.D., Patchett, P.J., Söderlund, U., and Baker, M. (2004) Isotopic composition of Yb and the
905 determination of Lu concentrations and Lu/Hf ratios by isotope dilution using MC-ICPMS.
906 *Geochemistry Geophysics, Geosystems*, 5, Q11002.
- 907 Wood, B.J., Kiseva, E.S., and Matzen, A. (2013) Garnet in the Earth's mantle. *Elements*, 9, 6, 421-426.
- 908 Yakymchuk, C., and Brown, M. (2014) Behaviour of zircon and monazite during crustal melting. *Journal*
909 *of the Geological Society, London*, 171, 465–479.

910 **FIGURES**

911

912 Figure 1. Simplified geological map of northern and central Fiordland showing the Western
913 Fiordland Orthogneiss and adjacent rocks, New Zealand. The migmatitic granulite sample
914 09NZ22 is shown on Crooked Arm. Map inset shows Fiordland along the southwest edge of the
915 South Island New Zealand. Fiordland geology is modified from Allibone et al. (2009) and
916 Turnbull et al. (2010). Worsley = Worsley Pluton; E McKerr = Eastern McKerr Intrusives; W
917 McKerr = Western McKerr Intrusives; Misty = Misty Pluton; Malaspina = Malaspina Pluton;
918 Breaksea = Breaksea Orthogneiss; DSSZ = Doubtful Sound shear zone. Pluton ages are zircon
919 U-Pb results reported in Schwartz et al. (2017).

920

921 Figure 2. Photographs of the Malaspina Pluton along Crooked Arm, New Zealand. (a) Ductile
922 folds in diorite gneiss and hornblende pyroxenite layers west of 09NZ22. These folds are
923 tentatively interpreted as D₃. (b) Garnet granulite with leucosome vein which cuts the LS fabric
924 in a wide garnet reaction zone and is bordered by a selvage of 10 to 12 mm euhedral garnet,
925 09NZ22. Leucosome and garnet reaction zone (09NZ22A), and host (09NZ22B) samples
926 discussed here include this vein, garnet selvage, and garnet reaction zone. Fabric correlations are
927 with those from Klepeis et al. (2016). (c) Photomicrograph of host orthogneiss in sample
928 09NZ22b. Note well-developed foliation in this two pyroxene diorite. (d) Photograph of the
929 garnet reaction zone in sample 09NZ22a. Type 2 garnet grains form a selvage along the
930 leucosome vein in the upper right. Type 1 garnet are intergrown with clinopyroxene in the lower
931 left part of the photograph. Lines indicate the locations for the EPMA garnet compositions
932 presented in Figure 8 and the arrowheads indicate the right hand end of the zoning profiles. GRZ
933 = garnet reaction zone.

934

935 Figure 3. Cathode luminescence images of zircon from migmatite in 09NZ22, Crooked Arm
936 New Zealand. (a) Zircon from orthogneiss host, 09NZ22b. (b) Zircon from garnet reaction zone
937 adjacent to trondhjemite vein, 09NZ22a. Circles indicate position of SHRIMP-RG U-Pb analyses,
938 top number is grain and analysis number, and bottom number is age and 2σ uncertainty in Ma.

939

940 Figure 4. U-Pb CA-ID-TIMS ages determined for chemically annealed zircon from 09NZ22
941 migmatite, Crooked Arm New Zealand. (a) Concordia plot showing the error-weighted ellipses
942 for zircon from host (dashed lines) and garnet reaction zone (solid lines). (b) Comparison of the
943 ²³⁸U-²⁰⁶Pb zircon ages for the same data shown in (a). Note the significant overlap between host
944 and GRZ zircon ages and the single outlier at 115.70 Ma. (c) Photograph of host zircon grains
945 analyzed by CA-ID-TIMS. (d) Photograph of garnet reaction zone zircon grains analyzed by CA-
946 ID-TIMS.

947

948 Figure 5. U-Pb ages determined from SHRIMP-RG analysis of zircon from 09NZ22 migmatite,
949 Crooked Arm New Zealand. (a) Tera Wasserburg concordia plot showing error ellipses and
950 spread of ages along concordia. All but one of the host ages are concordant within uncertainty. (b)
951 All the 29 ²³⁸U-²⁰⁶Pb zircon ages shown in (a) have a weighted mean age of 116.7±1.4 Ma with
952 an MSWD of 12.3. Separation of the ages into garnet reaction zone and Host also produces
953 weighted mean ages with high MSWD; however, removal of the oldest ages from each dataset

954 results in weighted mean ages that overlap at 2σ uncertainties and have MSWD values <2.5 :
955 GRZ = 119.8 ± 1.2 and Host = 117.9 ± 0.9 Ma. The 8 younger ages, shown in gray extend down to
956 and overlap with garnet ages and are interpreted to result from Pb loss.

957
958 Figure 6. Sm-Nd and Lu-Hf isochron ages for garnet reaction zones in migmatite from Crooked
959 Arm New Zealand. (a) Garnet and whole rock Sm and Nd isotope results. Note the ca. 8 m.y.
960 difference between the age for a single aliquot at ca. 112 Ma (solid line) and the other aliquots at
961 ca. 104 Ma (dashed line). The 112 Ma age is within uncertainty of the age for large garnet ca.
962 113 Ma in this sample (Stowell et al., 2014). (b) Garnet and whole rock Lu and Hf isotope results.
963 Note the large difference between the isochron for seven garnet fractions ca. 115 Ma (solid line)
964 and for seven garnet fractions with whole rock ca. 111 Ma (dashed).

965
966 Figure 7. Zircon trace element compositions in migmatite from Crooked Arm New Zealand
967 measured using SHRIMP-RG. Trace element data for zircon with spot ages less than 115 Ma
968 were excluded due to possible metamorphic origin. The host and garnet reaction zone zircon
969 form separate field with limited overlap. The similar Th/U and HREE values at low Hf
970 concentrations are compatible with a single magma source for the Host and garnet reaction zone;
971 however, trends indicate significantly greater fractionation for host rock.
972 (a) Sm versus Hf in zircon. Inset shows the lack of a trend in U-Pb zircon age versus Hf. (b) Yb
973 versus Hf in zircon. (c) Yb/Dy versus Hf in zircon. (d) Ce/Ce* versus Hf in zircon. Ce* = Ce
974 predicted from slope of line between adjacent REE. (e) Eu/Eu* versus Hf in zircon. Eu* = Eu
975 predicted from slope of line between adjacent REE. (f) Th/U versus Hf in zircon. (g) Yb versus
976 Th/U in zircon. (h) Chondrite-normalized REE values for zircon. Steep curves for Host and
977 garnet reaction zone indicate that zircon was not in equilibrium with garnet during growth.
978 Chondrite normalization values are from McDonough and Sun (1995).

979
980 Figure 8. Garnet compositions in migmatite sample 09NZ22 from Crooked Arm New Zealand.
981 (a) Mole fractions of almandine (Alm), pyrope (Prp), spessartine (Sps), and grossular (Grs) in
982 large (~ 1 cm) garnet from vein selvages in sample 09NZ22a. Small garnet in the selvages lack
983 high Sps cores and show limited zoning that mimics the outermost rims of large grains. (b) Sm
984 and Mn concentrations in large, ~ 10 mm diameter, selvage garnet. Data shown here were
985 extracted from maps in Stowell et al. (2014) and were obtained by laser ablation ICPMS. Data
986 “Thru Grt Center” are the from the middle row of a rectangular grid through the geometric center
987 of the grain. “Grt Off Center” are from row of analytical pits adjacent to center line. (c) Sm, Nd,
988 Yb, Lu, and Hf concentrations for the same large selvage garnet shown in (A). Neodymium and
989 Hf are unzoned or weakly zoned. Yb, Lu, and Hf have oscillatory zoning. Zirconium (not shown
990 for clarity) shows near identical oscillations to Yb. Data are a subset of those shown in maps
991 from Stowell et al. (2014) and were obtained by laser ablation ICPMS. (d) Sm, Nd, Yb, Lu, and
992 Hf concentrations in small, ~ 0.6 mm, GRZ garnet. Note the lack of systematic zoning in Nd and
993 Hf, and weak zoning in Sm and Lu with higher concentrations in the core, and similar, but more
994 pronounced zoning in Yb. Two sigma uncertainties are only shown for Nd for the sake of clarity.
995 However, 2σ uncertainties in Hf, Lu, Sm, and Yb are $\sim \pm 0.1$ ppm. Data were obtained by high
996 resolution Element 2 laser ablation ICPMS. (e) Chondrite-normalized REE values for garnet,
997 09NZ22. The steep slope from La to Gd and low slope from Gd to Lu at values from 20 to >100

998 are compatible with HREE sequestration into another mineral (see text for discussion). Chondrite
999 normalization values are from McDonough and Sun (1995).

1000

1001 Figure 9. Temperature and age estimates for zircon and garnet from 09NZ22, Crooked Arm NZ.
1002 (a) Temperature versus age. Garnet data include Lu-Hf and Sm-Nd ages from ~ 12 mm grains
1003 and Sm-Nd ages for small grains (Table 3). The temperature estimates for garnet growth are
1004 based on P-T pseudosections in Stowell et al. (2014). A best-fit line from garnet growth to Sm
1005 and Nd closure in the small garnet grains indicates a cooling rate of approximately 20°C/m.y.
1006 similar to the general trend of temperature versus age estimates for zircon temperatures. (b)
1007 Closure temperature estimates for Nd diffusion in garnet. Ti-in-zircon temperatures (Table 2)
1008 were calculated with Si activities of 0.8 and Ti activities of 0.7. All Ti in zircon temperatures are
1009 corrected to P=1.4 GPa using the dependence presented in Ferriss et al. (2008). Uncertainties for
1010 these Ti-in-zircon temperatures are likely to be > 60°C. Closure temperature estimates are based
1011 on the diffusion equations in Bloch et al. (2020), see Table 4.

1012

1013 Figure 10. Comparison of all age results for zircon and garnet in migmatite from 09NZ22,
1014 Crooked Arm New Zealand. The ten individual CA-TIMS zircon results are shown as solid
1015 circles, the older SHRIMP-RG zircon results are shown as a solid line indicating the range of
1016 weighted mean ages for GRZ and Host age populations, the younger SHRIMP-RG zircon age
1017 range is shown as a dashed line, The shaded area from 119 to 116.3 Ma shows the age range for 9
1018 of the 10 zircon CA-TIMS ages which overlap with the two older SHRIMP-RG age populations.
1019 This range is interpreted as the age of intrusion for the Malaspina Pluton in this part of Crooked
1020 Arm. The peak of metamorphism and garnet growth are taken as the overlap between Lu-Hf and
1021 Sm-Nd ages for large (~ 1 cm) grains. The thin dashed line at 104 Ma indicates the time for
1022 closure of small garnet grains to diffusion of Sm and Nd. The shaded gradient shows the
1023 interpreted age for garnet growth and the peak of garnet granulite metamorphism (115.4 to 111.3
1024 Ma) down to closure of small garnet to Sm and Nd diffusion (ca. 104 Ma).

1025

1026 Figure 11. Illustrations showing the 3 scenarios proposed for melt sources during garnet granulite
1027 metamorphism. (a) Partial melting of homogeneous Malaspina Pluton. (b) Injection of externally
1028 sourced leucocratic melt into a vein. (c) Partial melting of a felsic layer within the heterogeneous
1029 Malaspina Pluton. All of these three scenarios produce leucocratic veins, garnet selvages, and
1030 garnet reaction zones. The leucocratic veins are ~5 cm wide. See text for details. Red lines
1031 enclose areas of partial melt and the black dashed circles indicate two of the samples discussed in
1032 the text as host (09NZ22b) and garnet reaction zone (09NZ22a). Cpx = clinopyroxene, Grt =
1033 garnet, Hbl = hornblende.

1034

1035 **Tables**

1036

1037 Table 1. Zircon U-Pb isotope data, CA-TIMS from the Malaspina Pluton, Crooked Arm, NZ.

1038

1039 Table 2. Zircon U-Pb isotope data, SHRIMP-RG from the Malaspina Pluton, Crooked Arm, NZ.

1040

1041 Table 3. Garnet Sm-Nd and Lu-Hf isotope data from the Malaspina Pluton, Crooked Arm, NZ.

1042

1043 Table 4. Sm-Nd closure temperature estimates for garnet from the Malaspina Pluton, Crooked
1044 Arm, NZ.

1045

1046

1047 **Supplementary Tables**

1048

1049 Supplemental Table 1. Trace element concentrations in zircon, SHRIMP-RG. Malaspina Pluton
1050 09NZ22 Crooked Arm, NZ.

1051

1052

Table 1. U-Pb isotopic data for CA-ID-TIMS zircon analyses from the Malaspina Pluton, Crooked Arm, NZ

Sample Fractions	Pb(c) (pg)	Pb* Pb(c) (pg)	U (pg)	Th U	Ratios								Ages (Ma)						corr. coef.
					206 Pb 204 Pb	208 Pb 206 Pb	206 Pb 238 U	err	207 Pb 235 U	err	207 Pb 206 Pb	err	206 Pb 238 U	err	207 Pb 235 U	err	207 Pb 206 Pb	err	
					(d)	(e)	(f)	(2σ%)	(f)	(2σ%)	(f)	(2σ%)	(2σ)	(2σ)	(2σ)	(2σ)	(2σ)		
<i>Sample 09NZ22B: host orthogneiss</i>																			
z5	0.54	23.5	604	0.84	1302.5	0.268	0.018520	(.11)	0.12344	(1.03)	0.04836	(.99)	118.30	0.13	118.2	1.2	116	23	0.40
z4	0.53	21.3	557	0.76	1203.6	0.241	0.018409	(.10)	0.12339	(1.05)	0.04863	(1.02)	117.59	0.11	118.1	1.2	129	24	0.35
z3	0.54	9.1	233	0.89	510.9	0.284	0.018408	(.23)	0.12308	(2.83)	0.04852	(2.76)	117.59	0.26	117.9	3.2	123	65	0.38
z1	0.80	5.5	197	1.19	296.6	0.379	0.018269	(.37)	0.12220	(4.67)	0.04853	(4.54)	116.71	0.43	117.1	5.2	124	107	0.38
z2	0.63	21.6	613	1.16	1113.8	0.368	0.018267	(.11)	0.12246	(1.20)	0.04864	(1.17)	116.70	0.12	117.3	1.3	130	27	0.33
<i>Sample 09NZ22A: garnet reaction zone</i>																			
z2	0.54	8.8	234	0.75	510.2	0.240	0.018417	(.21)	0.12334	(2.57)	0.04859	(2.51)	117.65	0.25	118.1	2.9	127	59	0.33
z1	0.59	2.8	84	0.66	178.4	0.211	0.018394	(.62)	0.12405	(7.76)	0.04894	(7.56)	117.50	0.72	118.7	8.7	144	177	0.36
z3	1.19	11.8	724	0.58	703.9	0.183	0.018286	(.16)	0.12237	(1.91)	0.04856	(1.85)	116.81	0.18	117.2	2.1	125	44	0.37
z4	0.55	12.9	369	0.58	769.9	0.184	0.018245	(.14)	0.12220	(1.65)	0.04860	(1.61)	116.55	0.16	117.1	1.8	127	38	0.33
z5	1.64	11.2	949	0.60	664.8	0.191	0.018111	(.16)	0.12254	(1.90)	0.04910	(1.85)	115.70	0.18	117.4	2.1	151	43	0.34

Notes:

- (a) Thermally annealed and pre-treated single zircon.
 - (b) Total common-Pb in analyses. Pb* is radiogenic Pb content.
 - (c) Total sample U content.
 - (d) Measured ratio corrected for spike and fractionation only.
 - (e) Radiogenic Pb ratio.
 - (f) Corrected for fractionation, spike and blank. Also corrected for initial Th/U disequilibrium using radiogenic²⁰⁸Pb and Th/U_{mgm} = 2.8.
- Mass fractionation correction of 0.25%/amu ± 0.04%/amu (atomic mass unit) was applied to single-collector Daly analyses.
 All common Pb assumed to be laboratory blank. Total procedural blank less than 0.1 pg for U.
 Blank isotopic composition: ²⁰⁶Pb/²⁰⁴Pb = 18.15 ± 0.47, ²⁰⁷Pb/²⁰⁶Pb = 15.30 ± 0.30, ²⁰⁸Pb/²⁰⁶Pb = 37.11 ± 0.87.
 Corr. coef. = correlation coefficient.
 Ages calculated using the decay constants λ₂₃₈ = 1.55125E-10 y⁻¹ and λ₂₃₅ = 9.8485E-10 y⁻¹ (Jaffey et al. 1971).

Table 2. U-Pb zircon SHRIMP-RG isotopic analyses and error-weighted average ages Malaspina Pluton, Crooked Arm, NZ

Zrn Grain	Concentrations				Atomic Ratios ⁱ						Age (Ma)			Weighted Mean Age
	Ti (ppm)	U (ppm)	²³² Tl/ ²³⁸ U	²⁰⁶ Pb ⁱⁱ (ppm)	²³⁸ U/ ²⁰⁶ Pb ^{iv}	% err ± (1σ)	²⁰⁷ Pb/ ²⁰⁶ Pb ^{iv}	% err ± (1σ)	²⁰⁶ Pb/ ²³⁸ U ^v	% err ± (1σ)	T (°C) (Ti-Zrn)	²⁰⁶ Pb/ ²³⁸ U ^{vi}	err abs ± (2σ)	Age (Ma) ± (2σ)
GRZ														
GRZ-2.1	15	165	1.29	2.4	58.18	0.80	0.0490	5.1	0.01722	1.42	862	<i>109.8</i>	1.8	
GRZ-5.1	18	142	0.52	2.1	57.66	0.83	0.0465	5.7	0.01757	1.30	885	<i>111.1</i>	1.9	
GRZ-4.2	33	120	0.67	1.8	57.22	0.91	0.0442	10.5	0.01735	1.60	956	<i>112.3</i>	2.4	
GRZ-3.1	26	226	0.49	3.5	55.68	0.73	0.0477	4.4	0.01798	1.00	925	<i>114.8</i>	1.7	
GRZ-9.1	13	261	0.58	4.1	54.98	0.70	0.0479	4.0	0.01821	0.87	850	<i>116.3</i>	1.7	
GRZ-7.1	16	158	0.54	2.5	54.60	0.81	0.0534	4.8	0.01835	1.15	873	<i>116.3</i>	2.0	
GRZ-1.1	14	185	0.71	2.9	54.72	0.77	0.0450	4.9	0.01820	1.04	858	<i>117.2</i>	1.9	
GRZ-12.1	24	96	0.88	1.5	54.53	1.09	0.0465	6.8	0.01807	1.91	918	<i>117.4</i>	2.6	
GRZ-4.1	16	277	0.56	4.4	54.16	1.14	0.0462	3.9	0.01852	1.22	870	<i>118.3</i>	2.7	
GRZ-8.1	23	234	0.48	3.8	53.32	0.72	0.0478	4.1	0.01882	0.92	910	<i>119.9</i>	1.8	
GRZ-12.2	27	223	0.46	3.6	53.07	0.78	0.0515	4.1	0.01873	1.05	929	<i>119.9</i>	1.9	
GRZ-13.1	30	238	0.47	3.9	52.97	0.71	0.0474	4.1	0.01894	0.85	946	<i>120.7</i>	1.8	
GRZ-10.1	16	265	0.56	4.3	53.00	0.70	0.0464	3.9	0.01885	0.91	870	<i>120.8</i>	1.7	
GRZ-14.1	27	123	0.52	2.0	52.83	0.88	0.0471	5.7	0.01904	1.27	931	<i>121.1</i>	2.2	
GRZ-6.1	32	177	0.49	2.9	52.50	0.78	0.0500	4.5	0.01907	1.16	953	<i>121.4</i>	2.0	
Host														
Host-10.1	14	278	1.05	4.1	58.11	0.71	0.0492	7.2	0.01719	0.88	855	<i>109.8</i>	1.8	
Host-12.1	26	278	0.44	4.2	57.17	0.69	0.0491	3.9	0.01734	0.95	927	<i>111.7</i>	1.6	
Host-5.1	25	156	0.87	2.4	56.01	1.51	0.0487	5.1	0.01776	1.91	922	<i>114.0</i>	3.4	
Host-8.1	15	222	0.90	3.5	54.83	1.44	0.0486	4.3	0.01835	1.56	860	<i>116.5</i>	3.3	
Host-7.1	36	192	0.81	3.0	54.68	1.42	0.0493	4.5	0.01817	1.66	968	<i>116.7</i>	3.3	
Host-13.1	36	225	0.47	3.5	54.49	0.73	0.0498	4.2	0.01833	0.90	968	<i>117.0</i>	1.8	
Host-15.1	13	138	0.79	2.2	54.45	1.71	0.0496	5.3	0.01826	1.94	845	<i>117.1</i>	4.0	
Host-3.1	42	190	0.93	3.0	54.15	0.83	0.0515	8.8	0.01833	1.20	988	<i>117.5</i>	2.3	
Host-9.1	18	153	0.88	2.4	54.14	1.62	0.0489	5.1	0.01838	1.94	882	<i>117.9</i>	3.8	
Host-14.1	35	218	0.46	3.5	54.08	1.15	0.0487	4.2	0.01838	1.35	963	<i>118.1</i>	2.7	
Host-4.1	16	145	0.89	2.3	54.05	0.83	0.0487	5.3	0.01847	1.37	869	<i>118.1</i>	2.1	
Host-6.1	30	173	0.92	2.8	53.69	0.79	0.0498	4.8	0.01854	1.07	942	<i>118.7</i>	1.9	
Host-11.1	35	238	0.47	3.8	53.99	0.77	0.0392	4.6	0.01862	1.16	964	<i>119.7</i>	1.9	
Host-2.1	49	147	0.85	2.4	52.75	1.42	0.0516	5.0	0.01866	1.77	1009	<i>120.6</i>	3.4	

ⁱErrors are % reported at 1σ level.ⁱⁱRadiogenic ²⁰⁶Pb.ⁱⁱⁱFraction of total ²⁰⁶Pb that is common ²⁰⁶Pb.^{iv}Uncorrected ratios.^v²⁰⁷Pb corrected ratios using age-appropriate Pb isotopic composition of Stacey and Kramers (1975).^{vi}²⁰⁷Pb corrected age. Spot analyses in italic were used to calculate the weighted average for the young age population.

Table 3. Sm, Nd, Lu, & Hf Isotope Data for Granulite in the Malaspina Pluton, Crooked Arm, NZ

Sample	[Sm] _{ppm}	[Nd] _{ppm}	¹⁴⁷ Sm/ ¹⁴⁴ Nd	2 SE	¹⁴³ Nd/ ¹⁴⁴ Nd	2 SE	Age (Ma) ± 2σ	Sample	[Lu] _{ppm}	[Hf] _{ppm}	¹⁷⁶ Lu/ ¹⁷⁷ Hf	2s (abs)	¹⁷⁶ Hf/ ¹⁷⁷ Hf	2s (abs)	Age (Ma) ± 2σ		
09NZ22a (P82421) 1 cm grain (Stowell et al., 2014)							113.1±2.2 ¹	10 pt	09NZ22a (P82421)							111.2±1.2	8 pt
09NZ22A-GRZ 0.5-2 mm diameter grains							103.6±2.2 ²	5 pt	WR B1	0.099	0.873	0.016119	0.000081	0.282971	0.000015		
WR	4.32	20.15	0.1296	0.0009	0.512651	0.000008		WR S1	0.093	0.839	0.015739	0.000079	0.282475	0.000020			
Mtx	1.46	8.99	0.0982	0.0007	0.512619	0.000008		Grt 2 Rim1 G2	2.509	0.475	0.749444	0.003747	0.284489	0.000015	114.8±3.5		
Cpx	8.74	37.93	0.1394	0.0010	0.512647	0.000009		Grt 2 Rim2 G3	2.506	0.532	0.668555	0.003343	0.284316	0.000015			
								Grt 2 Rim3 G4	3.049	0.511	0.846090	0.004230	0.284696	0.000015			
GX	3.78	3.28	0.6958	0.0049	0.513024	0.000008		Grt 2 Core2 G9	3.036	0.510	0.845221	0.004226	0.284702	0.000015			
GXfb	3.20	2.66	0.7262	0.0051	0.513055	0.000012		Grt 2 Rim1 2 G10	1.947	0.462	0.598138	0.002991	0.284163	0.000016			
								Grt 2 Rim2 2 G11	2.107	0.499	0.599703	0.002999	0.284176	0.000016			
GXfa	3.95	3.22	0.7427	0.0052	0.513094	0.000008	112.1±2.4 ³	4 pt	Grt 2 Rim3 2 G12	2.390	0.500	0.678888	0.003394	0.284341	0.000016		

Italic data are excluded from age calculations

¹Recalculated using IsoplotR

²GX and GXfb are multigrain aliquots used with WR, Mtx, & Cpx for age calculation

³GXfa was used with WR, Mtx, & Cpx for age calculation

Grt=garnet, Cpx=clinopyroxene, WR=whole rock (B= bomb dissolution, S= Savillex vial), Mtx=rock minus garnet

Table 4. Sm-Nd closure temperature estimates for garnet from the Malaspina Pluton, Crooked Arm, NZ

Sample	Cooling Rate (C/m.y.)	Garnet Radius mm	Diffusion Parameters	Closure T (°C)	Diffusion Parameters	Closure T (°C)
<u>09NZ22a (P82421)</u>			D(m ² /s) Nd ¹		D(m ² /s) Nd ²	
	-15	0.5-1.0	1.21E-20	690-740	3.00E-22	865-915
	-20	0.5-1.0		700-750		870-920
	-25	0.5-1.0		710-760		875-930
	-15	6		885		1060
	-20	6		900		1070
	-25	6		910		1080

Nd¹ from Bloch et al. (2020)

Nd² from Carlson (2012)

Figure 1

Major Intrusive Suites of Western Fiordland

Western Fiordland Orthogneiss

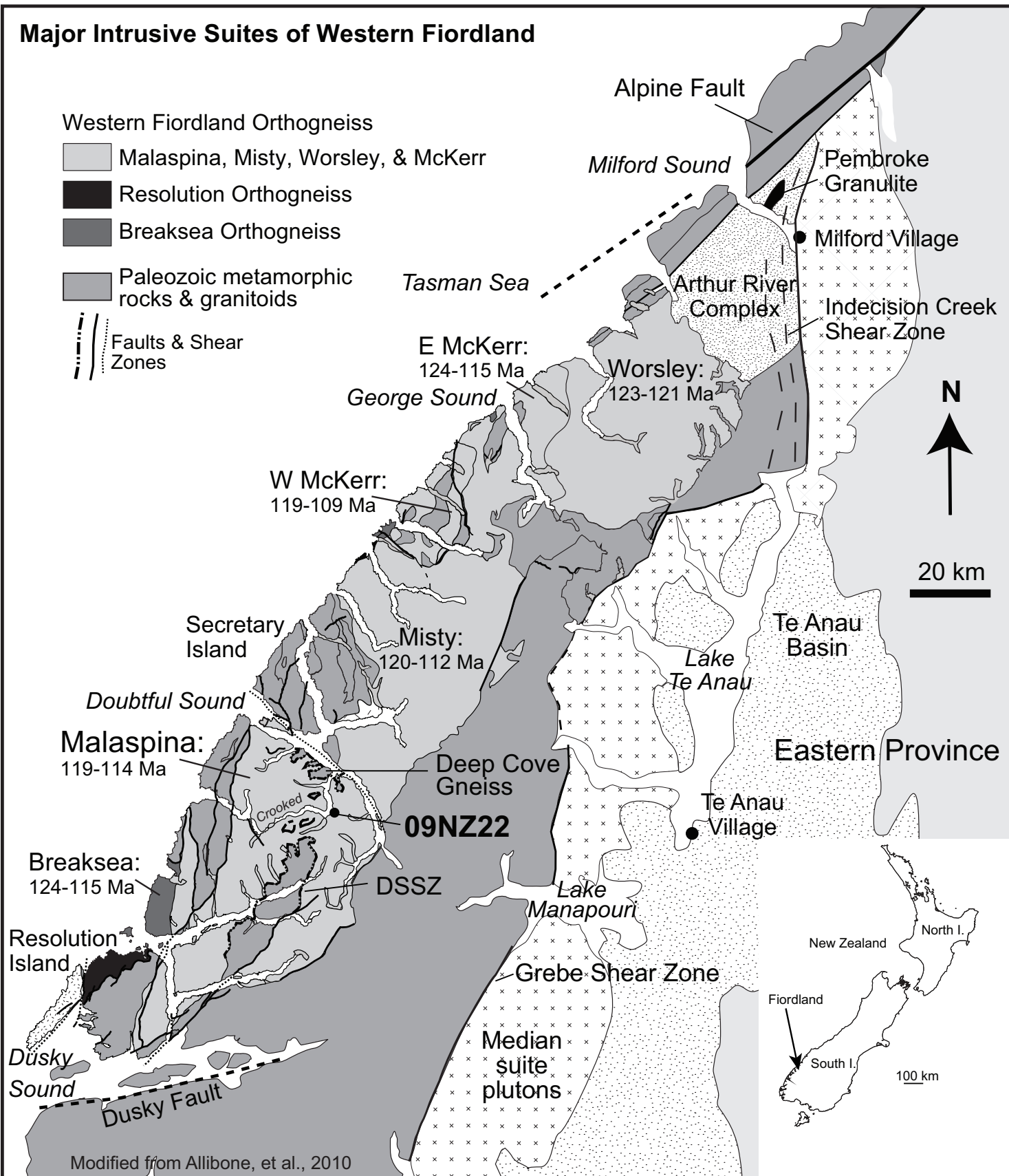
Malaspina, Misty, Worsley, & McKerr

Resolution Orthogneiss

Breaksea Orthogneiss

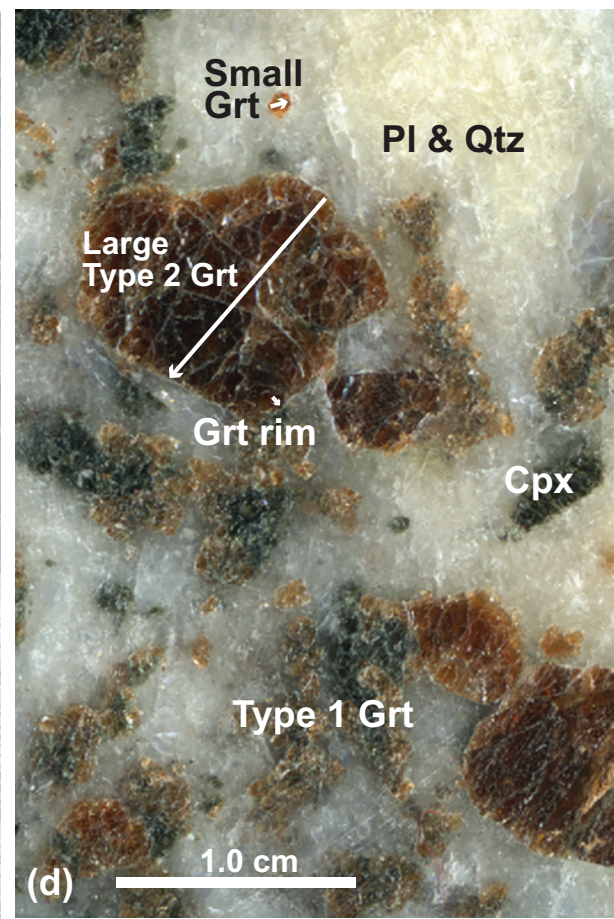
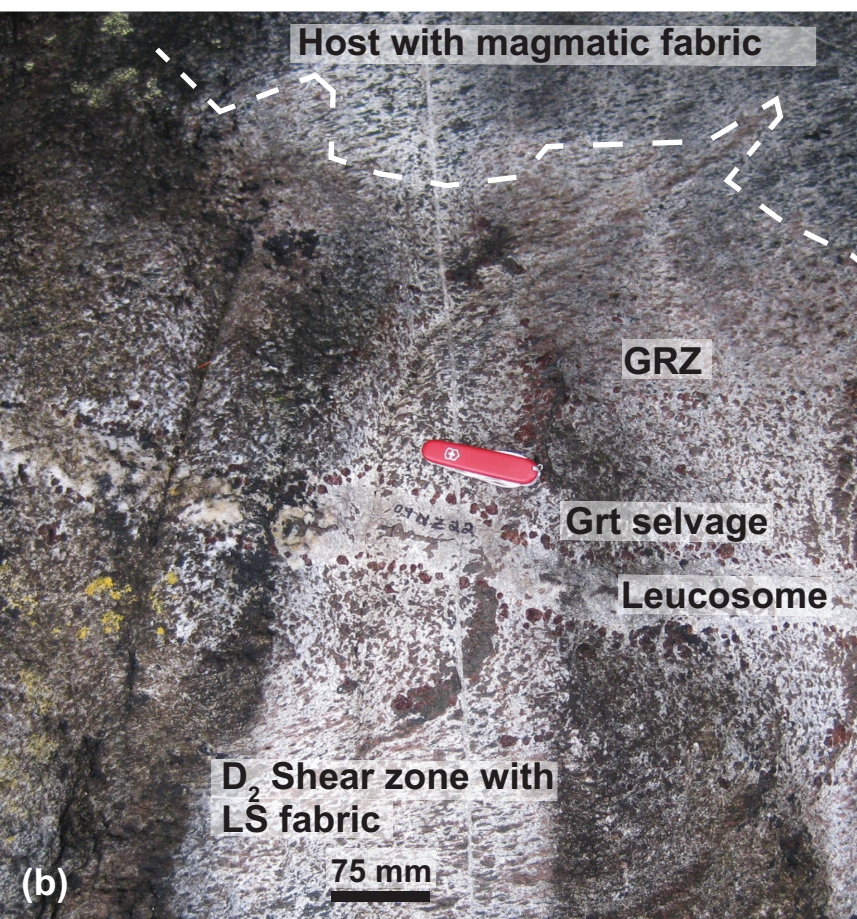
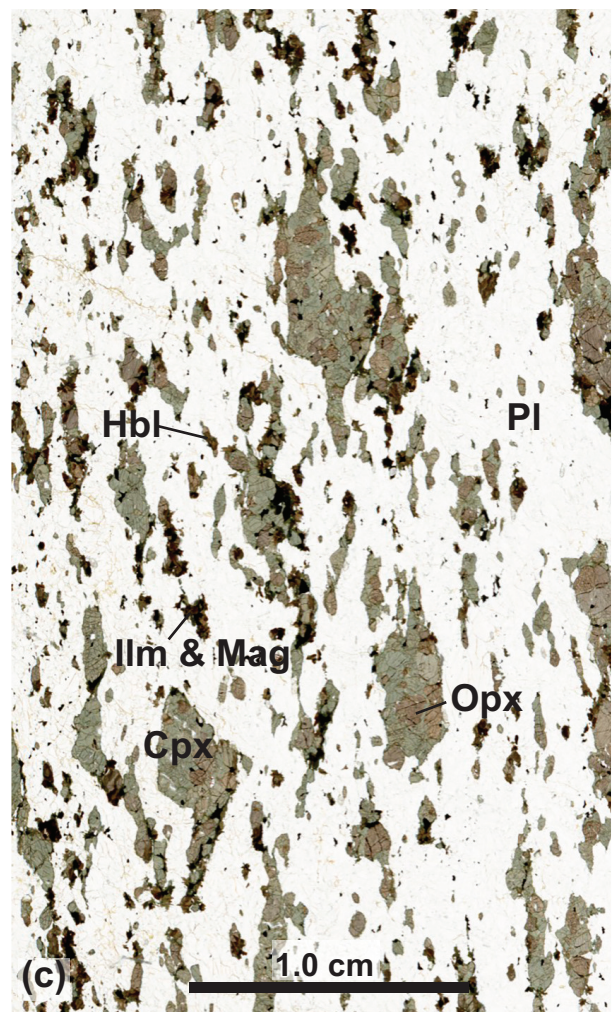
Paleozoic metamorphic rocks & granitoids

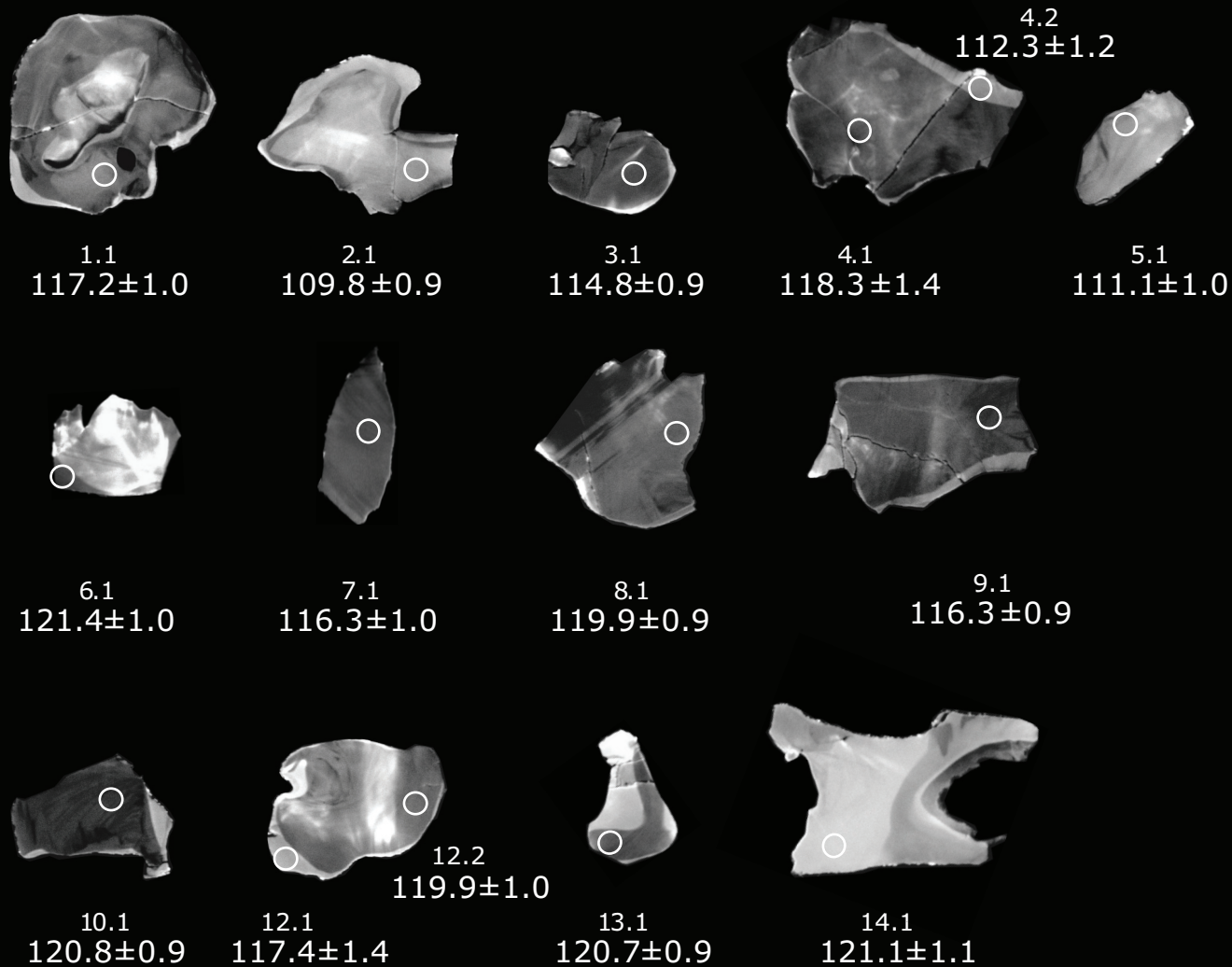
Faults & Shear Zones



Modified from Allibone, et al., 2010

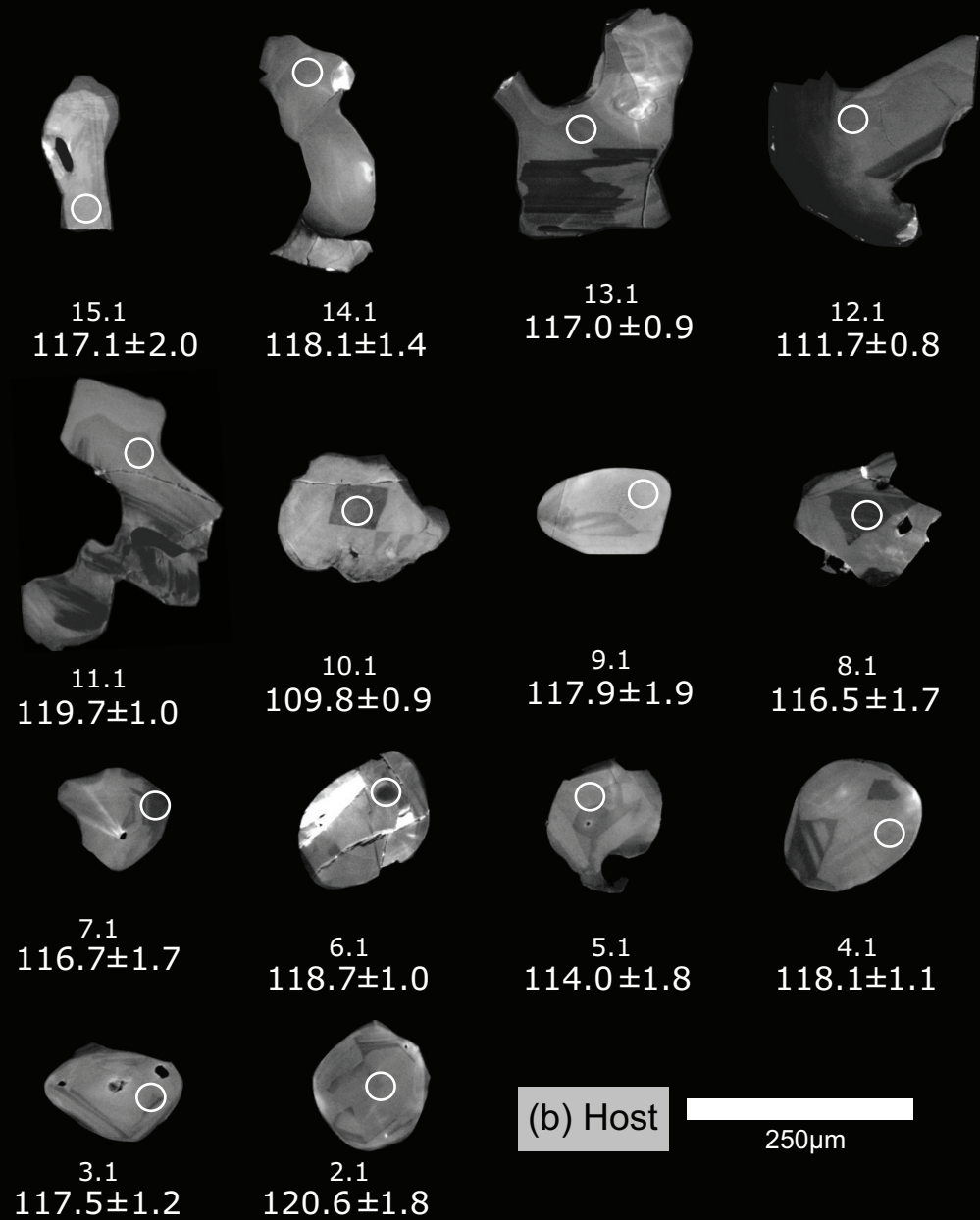
Figure 2





(a) Garnet Reaction Zone

250 μm

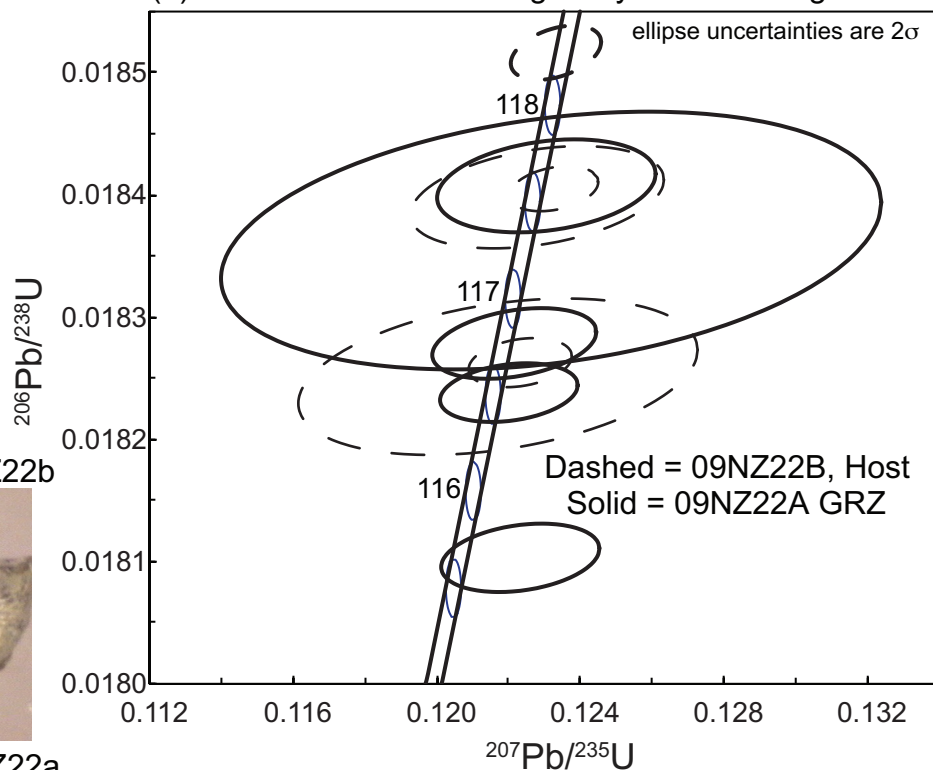


(b) Host

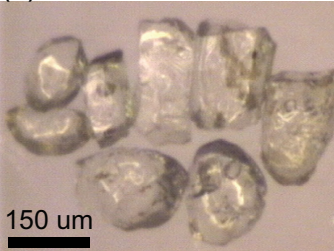
250 μm

Figure 4

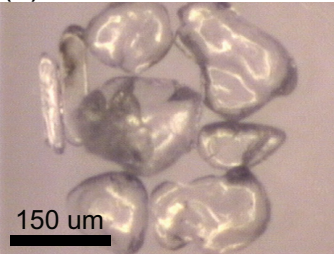
(a) Concordia Plot with Single Crystal Zircon Ages



(c) Zircon Host, 09NZ22b



(d) Zircon GRZ, 09NZ22a



(b) Comparison of Single Crystal Zircon Ages

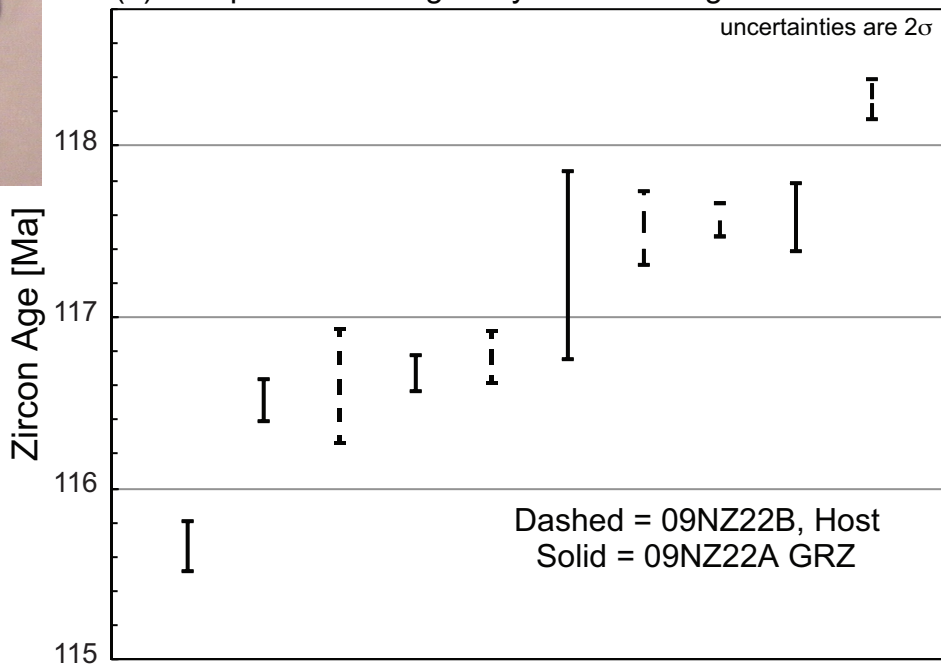


Figure 5

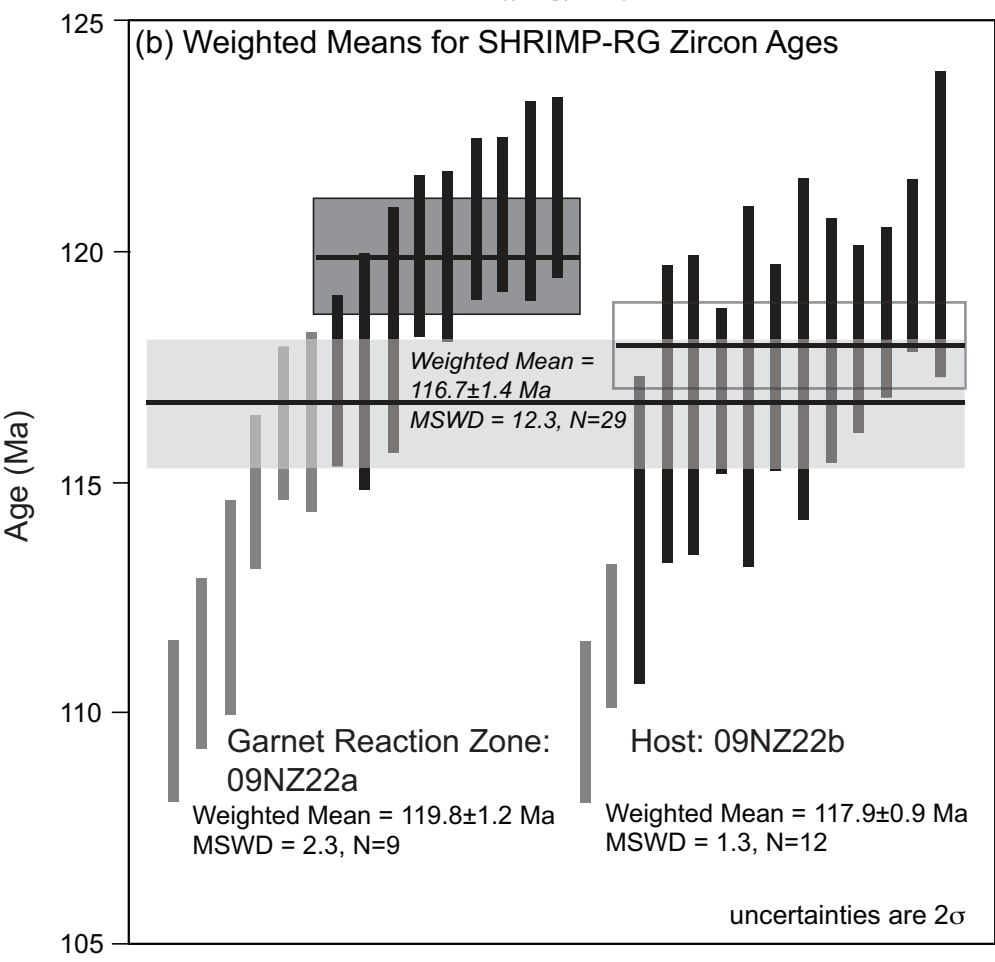
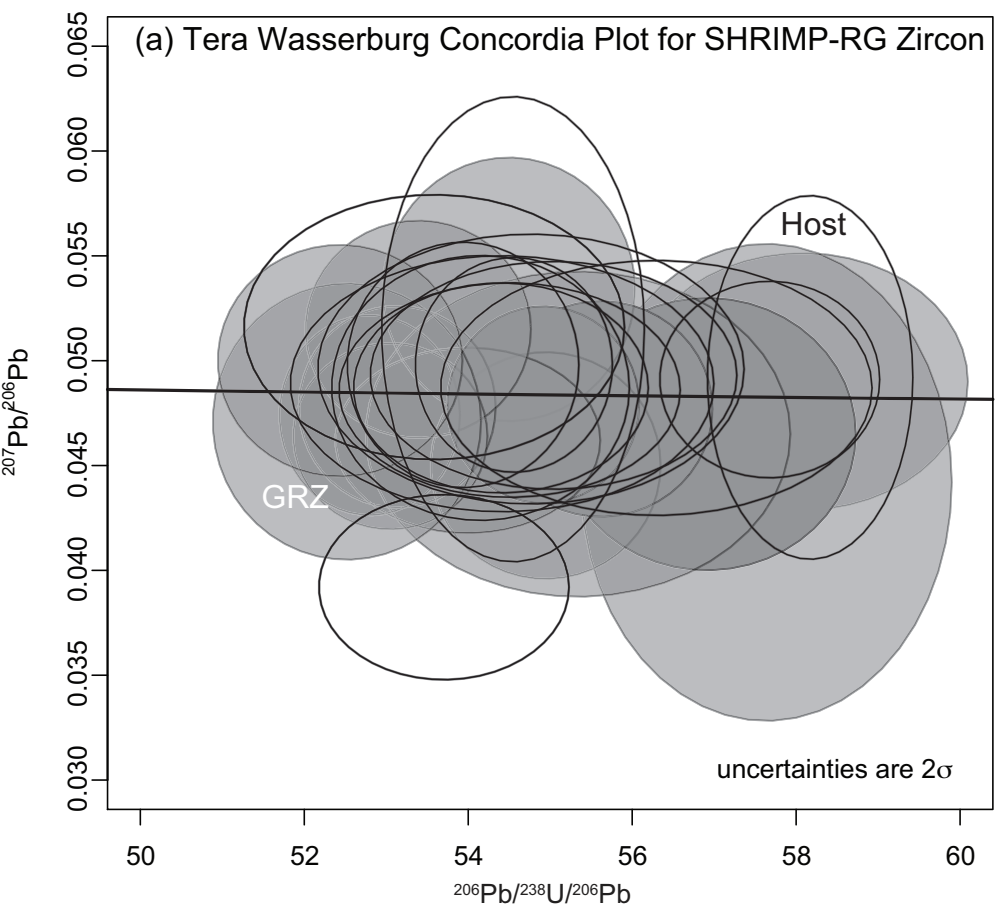


Figure 6

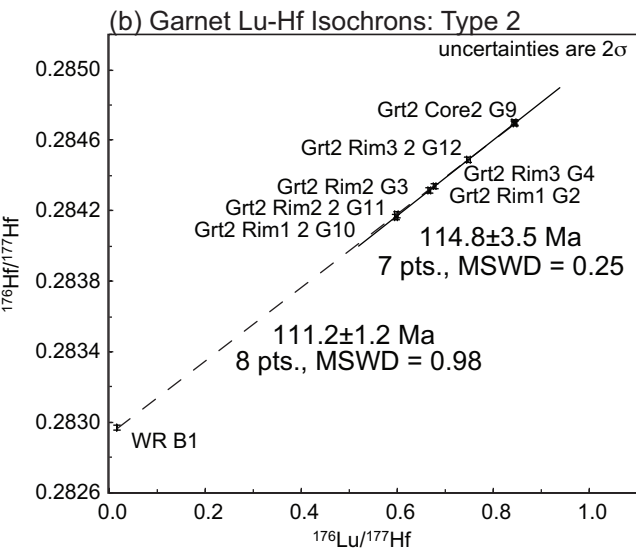
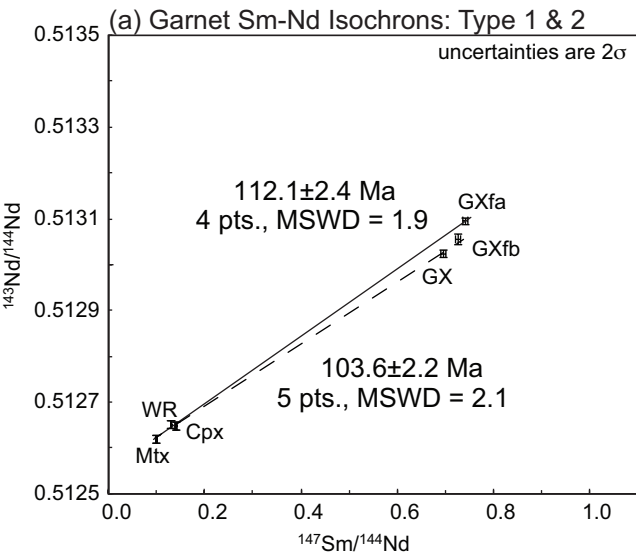


Figure 7

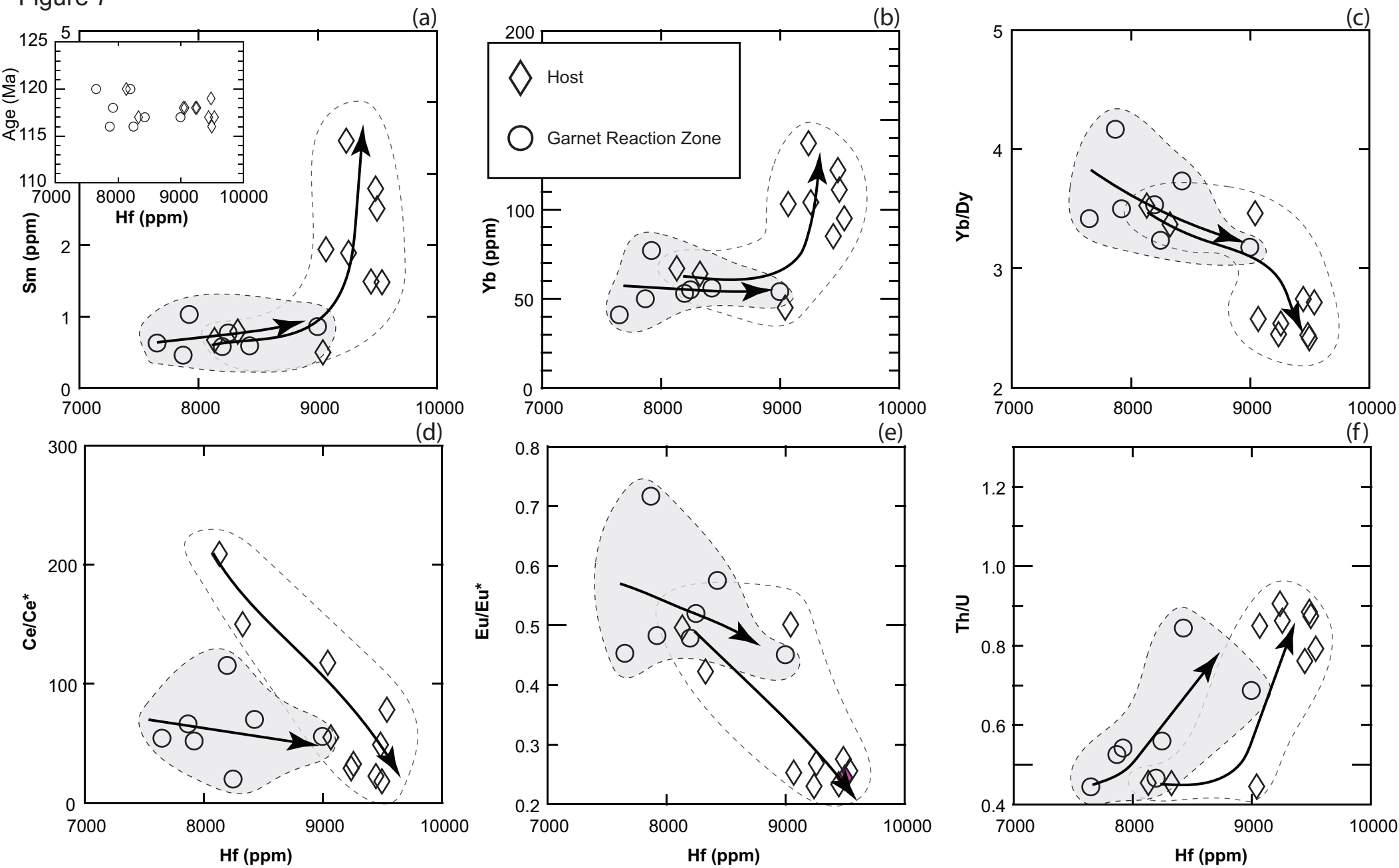
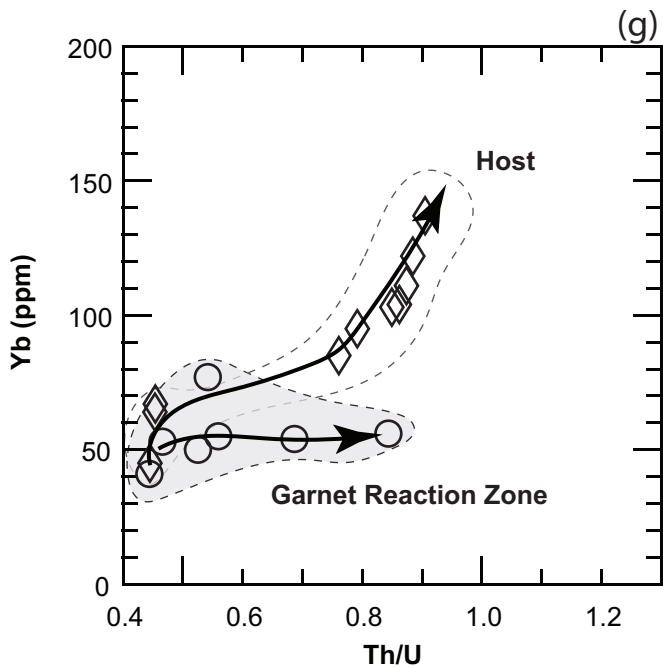


Figure 7gh



Rock/Chondrite

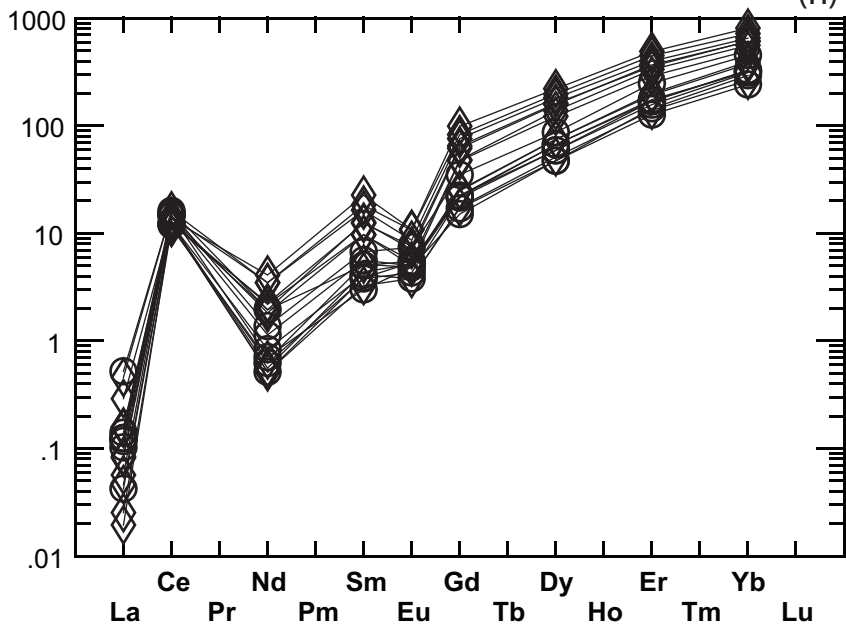


Figure 8a. Garnet major element zoning

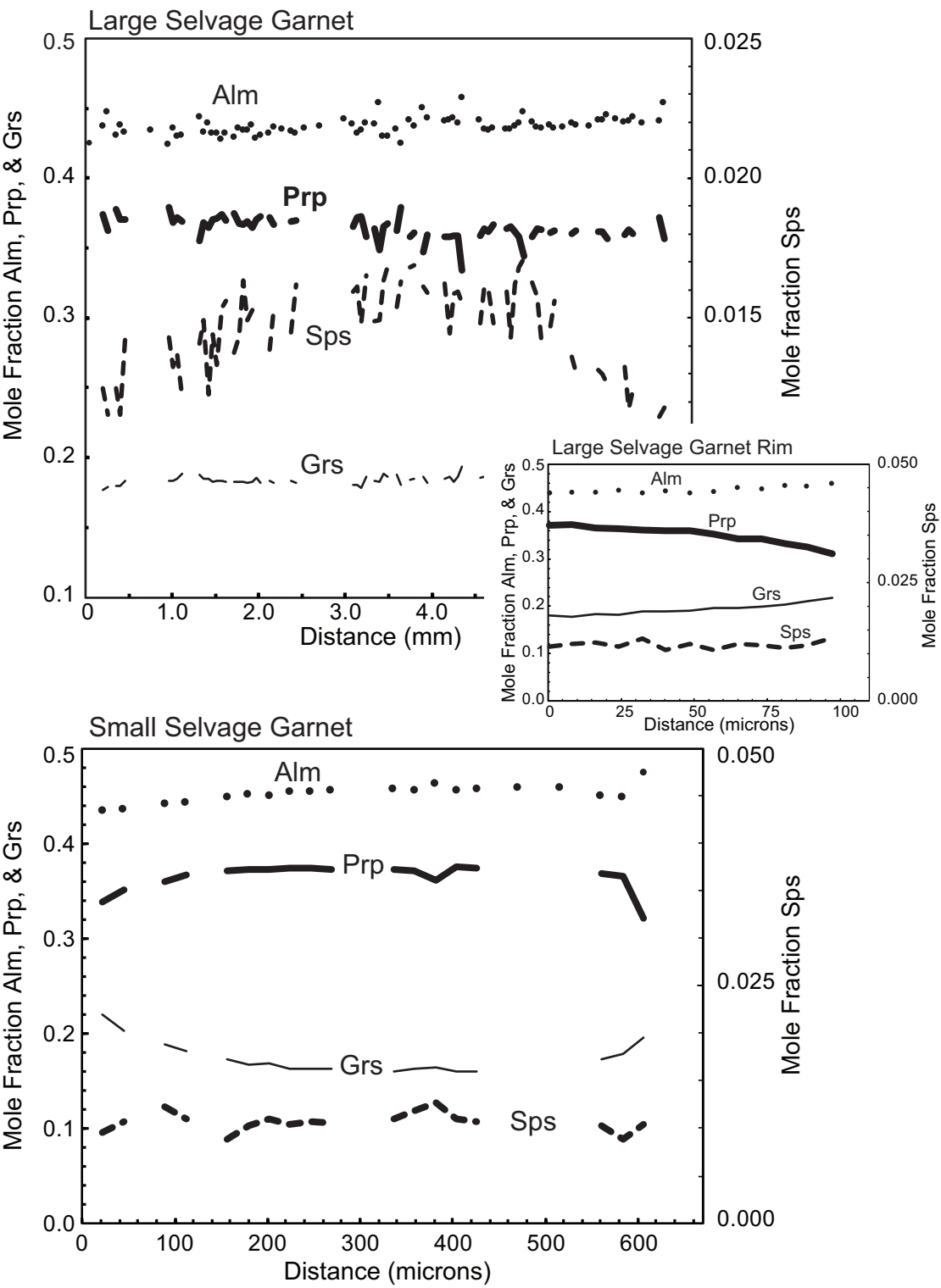


Figure 8bcd

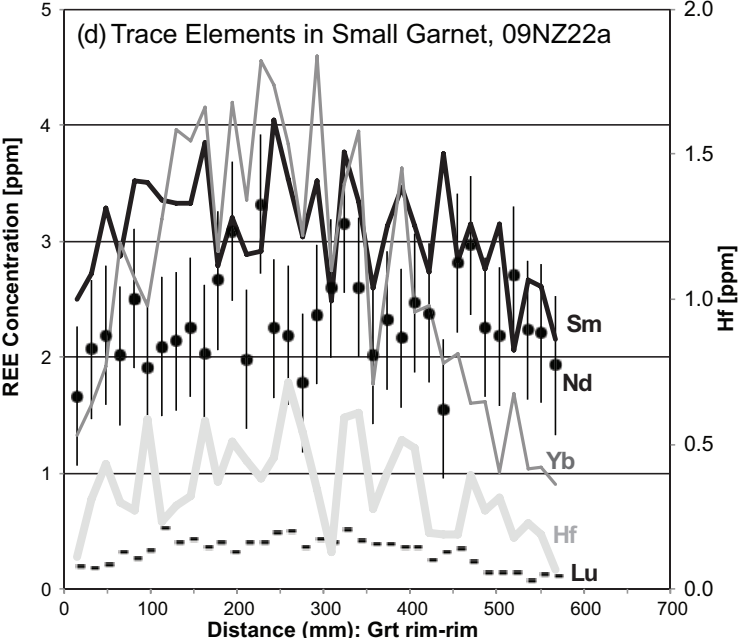
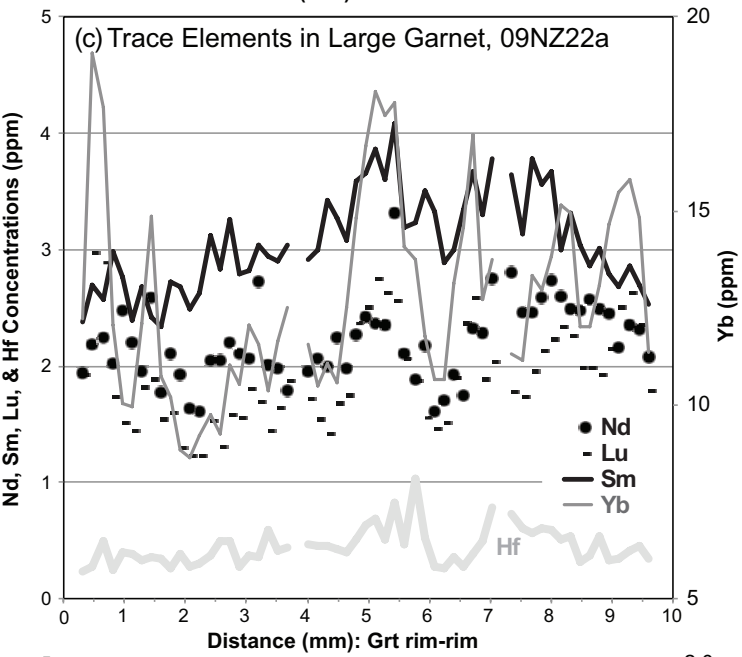
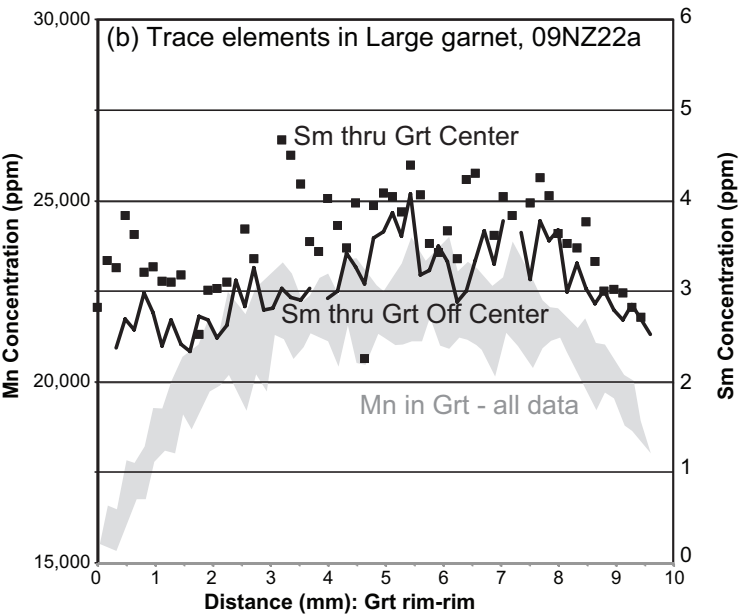


Figure 8e

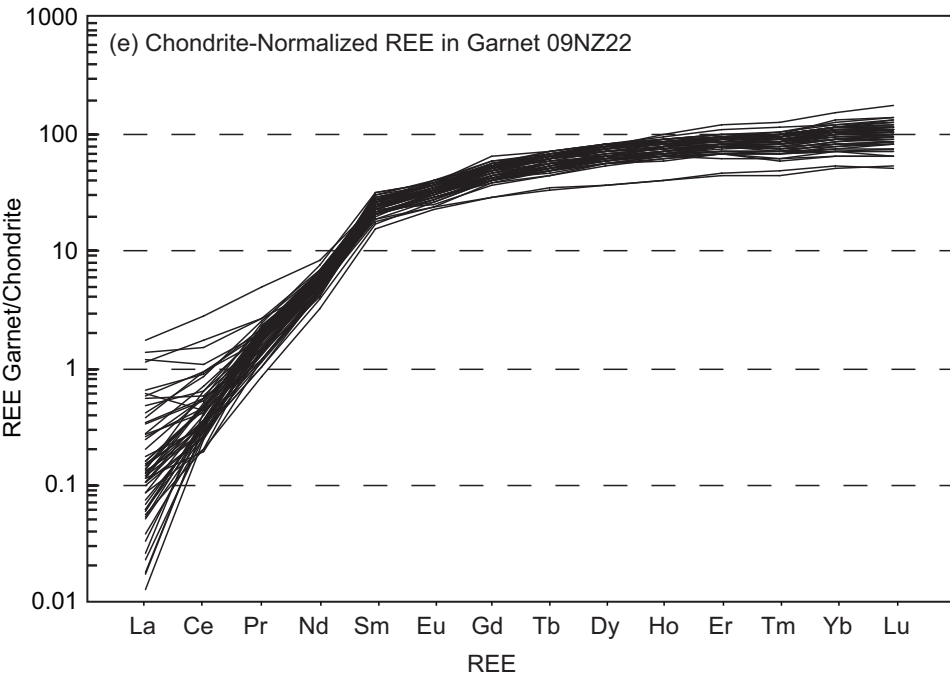
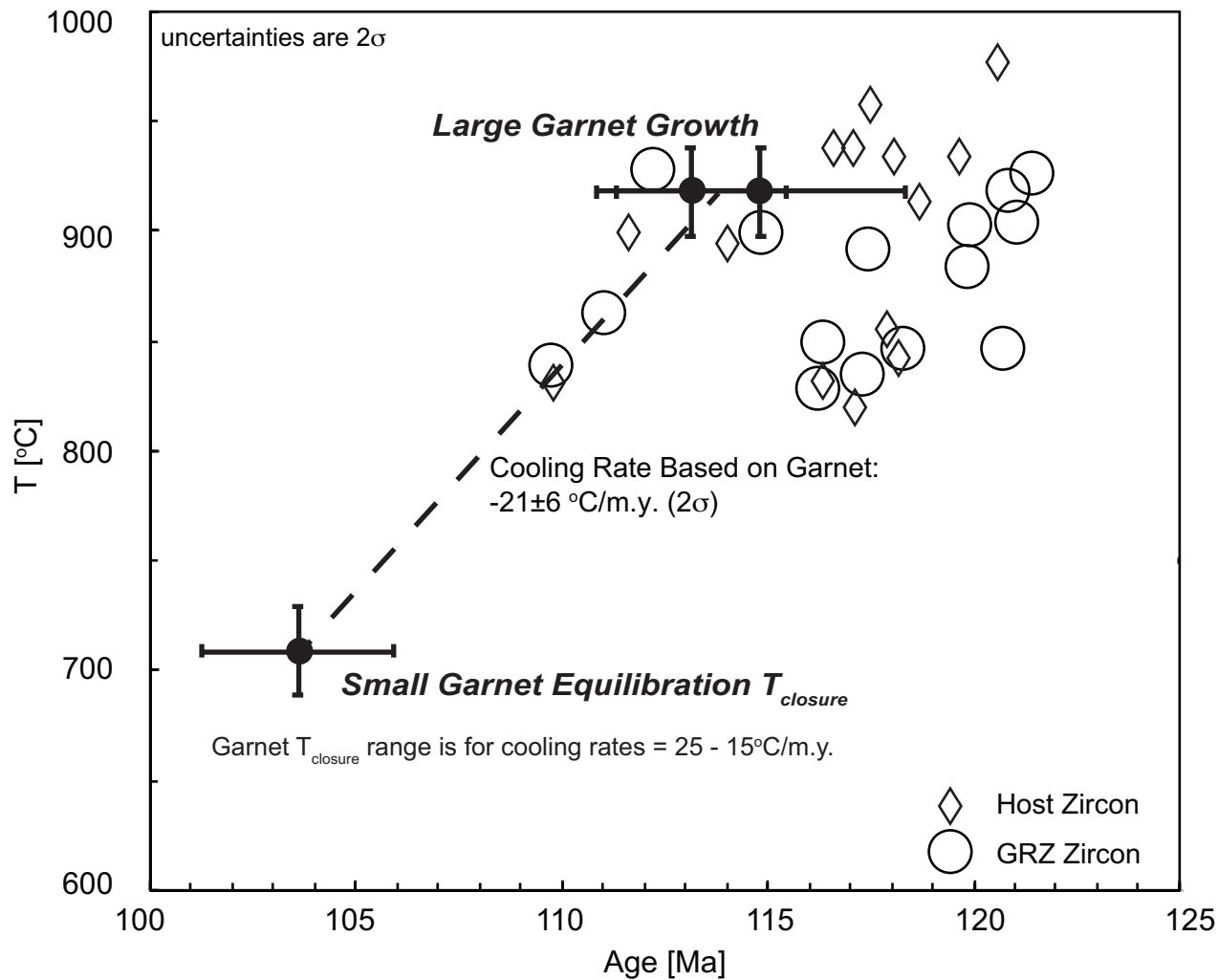


Figure 9

(a) Temperature vs. Age, O9NZ22



(b) Nd Closure Temperatures, Garnet

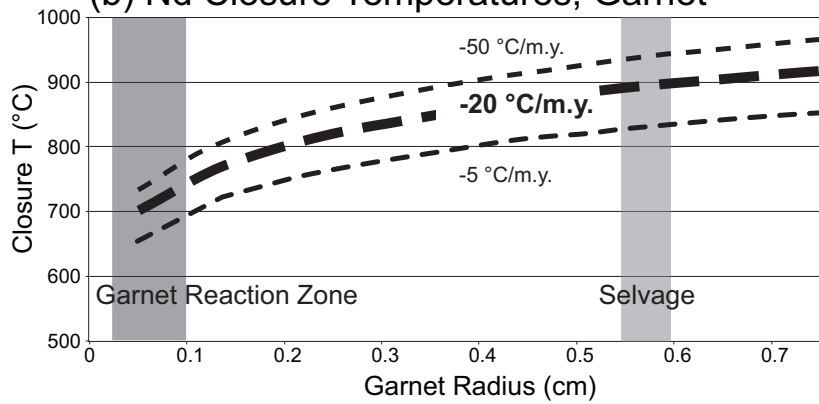
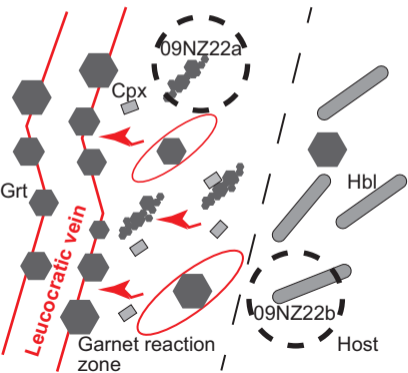
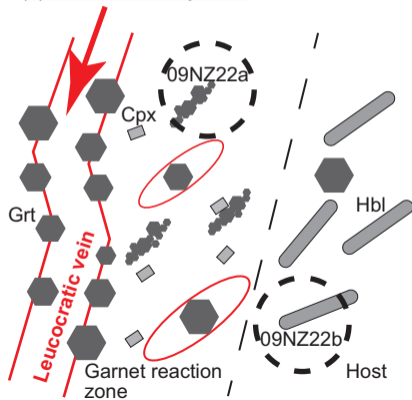


Figure 11

(a) Local Partial Melt: Homogeneous Pluton



(b) External Melt Injection



(c) Local Partial Melt: Heterogeneous Pluton

